ALMA MATER STUDIORUM A.D. 1088

UNIVERSITÀ DI BOLOGNA

DIPARTIMENTO DI SCIENZE BIOLOGICHE, GEOLOGICHE E AMBIENTALI

Corso di Laurea Magistrale in Geologia e Territorio

Raw Materials Exploration and Sustainability

Tesi di Laurea Magistrale

Amitsoq Graphite deposit, South Greenland: petrological and geochemical study of competing carbon and hydrogen storage processes

Candidato:

Giacomo Fratelli

Relatore:

Prof. Alberto Vitale Brovarone

Sessione luglio 2023

Anno Accademico 2022-2023

Abstract

The cycling of carbon and hydrogen in the Earth's lithosphere, including their geological storage, is complex. The Amitsoq graphite deposit provides an outstanding example of such processes. The Amitsoq graphite deposit is located in the Nanortalik region, South Greenland. It is one of the richest graphite deposits worldwide, with a JORC-resource estimate of more than 23 Mt at 20.41% graphitic carbon. The Amitsoq deposit was mined in the early 20th century, yet the origin of the carbon forming the graphite is presently unknown. The ore is hosted by two main bodies, namely the upper graphite level (UGL) and the lower graphite level (LGL), with the LGL being the thickest (up to 20m) and richest (typically 20-24% graphite). The ore bodies display a simple planar geometry, dipping 30° westward measured from the surface outcrops on the eastern flanks of Amitsoq Island. The deposit formed in the context of the ca. 1.8 Ga Ketilidian orogeny during the Paleoproterozoic, a geological period when the vast majority of the world's richest graphite deposits formed. The ore is hosted in amphibolite-facies psammite, which is thought to represent part of the fore-arc of the northward-dipping Ketilidian subduction zone and was formed by the erosion of the nearby Julianehåb batholith. Shortly after the orogeny, the area was intruded by several granitoid plutons. The combination of these factors led to high-temperature, low-pressure metamorphism with local anatexis. Tight folding observed in thin sections from the ore allows for the inference that graphite is either pre- or syn-kinematic with respect to the D_1-D_2 metamorphic events that occurred in the area. The ore is a graphite-sulphide schist in which graphite is present as millimetre scale, elongate flakes, often piled in stacks, and as cryptocrystalline agglomerates. Graphite flakes are interleaved with biotite and pyrrhotite and are variably folded. $\delta^{13}C$ analysis of graphite yields an average of -32‰ vs. PDB, compatible with biotic sources. $\delta^{34}S$ analyses yielded values ranging from 3‰ to 4‰, a range that overlaps with several possible sources. Thermometry studies yield temperatures of ~500 °C and ~575 °C ± 50 °C. Several models are proposed to explain the deposition of graphite under the conditions described in the literature and inferred from thermometry. This case study also showed possible evidence of the interaction between hydrogen and graphite, a process that generates methane, an aspect that has to be taken into account while considering carbon and hydrogen storage processes.

Contents

Table of figures

1. Introduction

The Amitsoq graphite deposit is situated in the southern region of Amitsoq Island, approximately 15 km north of Nanortalik in the Southern Domain of the Ketilidian Orogen in SW Greenland (Kolb et al., 2016). Mining operations at the Amitsoq mine commenced in 1914 with an initial excavation of around 130 tons of graphite ore, followed by two batches of 2000 tons in 1915. After a pause during World War I, mining activities resumed, but only 571 tons of graphite concentrate were produced between 1918 and 1921, and exploitation ceased in 1922 (Ball, 1923). The estimated ore reserves were calculated to be 250,000 tons (Bondam, 1992), but only 6000 tons of graphite ore were actually mined (Nielsen, 1973). A more recent JORC-resource estimate suggests a resource exceeding 23 million tons with a graphitic carbon content of 20.41%. Despite being known for over a century, little is known about the formation conditions and origin of this deposit.

The objective of this study is to characterise and understand the petrology and geochemistry of the Amitsoq graphite deposit, with a particular focus on precipitation mechanisms of graphite, such as dehydration, fluid mixing, and temperature change (Frost, 1979; Rumble & Hoering, 1986), as well as the generation of hydrogen in natural systems. The study aims to test the hypotheses of hydrogen production through serpentinization (Sherwood et al., 2007), pyrite formation (Drobner et al., 1990), and radiolysis (Lin et al., 2005; Sherwood et al., 2014).

Initially, a comprehensive review of existing literature was conducted to explore the Ketilidian orogeny and its relation to the metamorphic history of the study region in South Greenland. This examination aimed to determine if previous studies have addressed similar geological contexts and documented relevant metamorphic, metasomatic, and mineralizing events in the area. The studied area is located on Amitsoq Island, which is part of the Nanortalik nappe, a sequence of meta-sedimentary rocks, banded quartz-graphite-sulphide rocks, and variably metamorphosed mafic volcanic rocks thrust over the meta-sedimentary rocks (Petersen et al., 1997; Kaltoft et al., 2000).

In the second chapter a brief description of the geological background is presented, explaining that the Nanortalik nappe is part of the Pelite/Psammite zone (Bell et al., 2017), which comprises a series of metasedimentary rocks formed from the metamorphism of sediments eroded from the unroofing of the Julianehåb batholith in the context of the 'Andean type' Ketilidian orogeny (Chadwick & Garde, 1996).

In the third chapter, the methods used in this study are presented, while in the fourth chapter a detailed petrographic analysis is shown with a description of samples from the ore, host rock, and nearby granitoid bodies closely associated with the deposit. These observations allowed for the identification of key petrographic characteristics of the deposit, determination of mineral distribution within the samples, and observation of graphite occurrence in various lithological units.

Following the petrographic observations, a more detailed geochemical study was conducted using electron microprobe (EMPA; chapter 4.2) and μ-X-ray fluorescence (μ-XRF; chapter 4.3). These techniques facilitated the examination of element distribution through the creation of element maps and enabled a thorough analysis of individual mineral phases,

including thermobarometry calculations. Additionally, in chapter 4.4 X-ray diffraction was employed to confirm the mineralogy of the ore.

Raman spectroscopy was utilised to infer the peak metamorphic conditions during graphite formation and to analyse the composition of fluid inclusions in the ore and the host rock. This technique revealed intriguing findings when examining the composition of fluid inclusions in both the ore and the host rock. Particularly, the absence of CO_2, the prevalence of CH_4, and the presence of H_2 were among the notable observations.

The analysis of stable carbon isotope fractionation in chapter 4.6 played a critical role in understanding the origin and modelling of carbon within the deposit. It was inferred that the carbon likely originated from biotic sources. Conversely, the analysis of stable sulfur isotopes yielded somewhat ambiguous results and did not provide clear evidence regarding the possible source of sulfur.

All these analyses and considerations were employed to provide a plausible explanation for the formation of the deposit and the processes involved in the entrapment of carbon and hydrogen within it.

The relevance of this study goes beyond the academic aspects of understanding the geological processes that brought to the formation of the Amitsoq graphite deposit but it also delves into considerations relevant for critical raw materials fundamental in the electric vehicle batteries' market, such as graphite (Anthony et al., 1990; Taylor, 2006), a possible natural source of hydrogen, which may be an important future player as energy carrier in the green transition (Ahluwalia & Peng, 2009), and the effects of the interaction between carbon and hydrogen in natural systems.

2. Regional Geology

The Amitsoq graphite deposit is located in South Greenland, a region which comprises three main tectono-stratigraphic domains: (1) the Archaean basement, (2) the Palaeoproterozoic Ketilidian orogen, and (3) the Mesoproterozoic Gardar alkaline igneous province, as well as volumetrically negligible Phanerozoic rocks (Steenfelt, 2016). Compared to other Greenlandic orogens (e.g., Rinkian, Nagssugtoqidian and Ammassalik) in the Ketilidian orogeny there is no involvement of Archan crust (Chadwick and Garde, 1996).

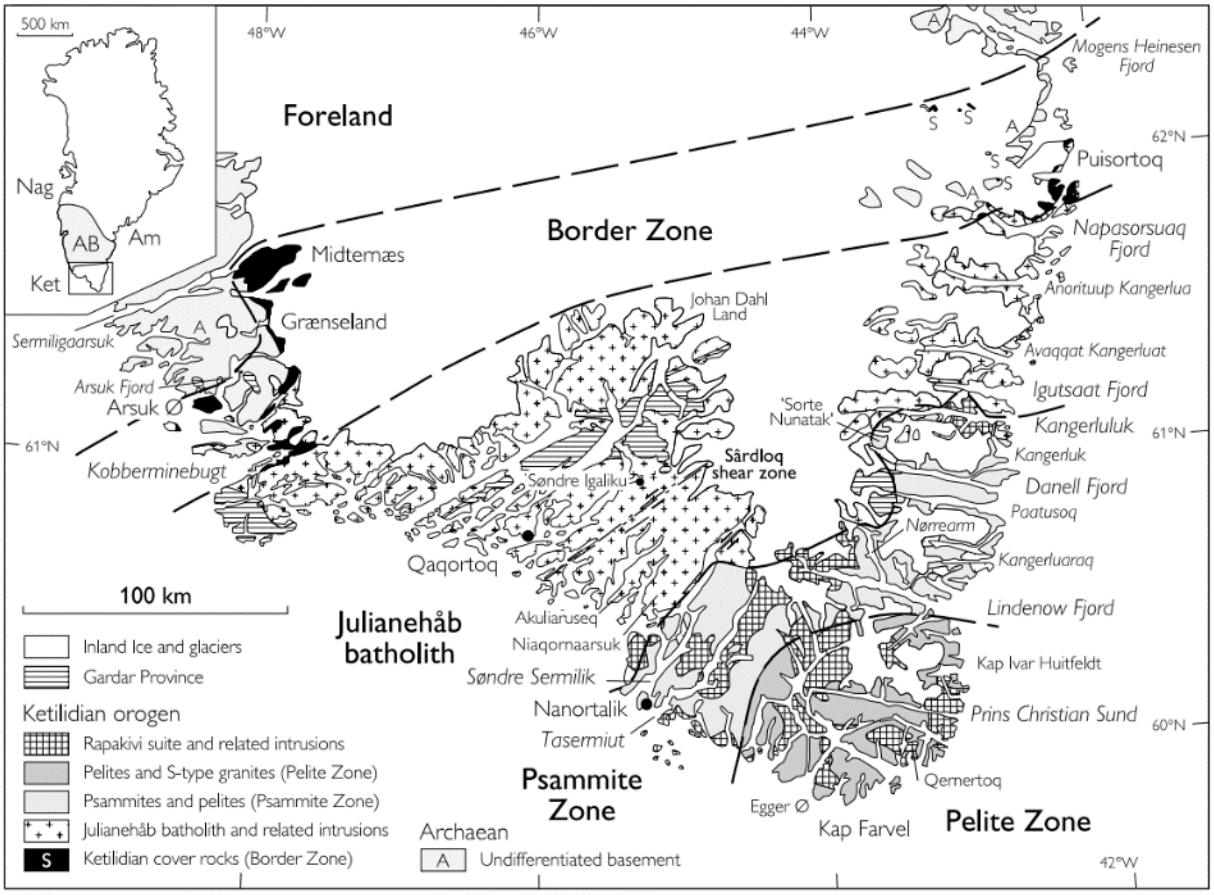

Figure 1: Geology of South Greenland (Garde et al., 2002).

The Ketilidian Orogen, which takes its name from the Ketilis Fjord (now called Tasermiut Fjord; Figure 1; Wegmann, 1938), is an important component of the system of Paleoproterozoic mobile belts in North Atlantic region and is one of four major orogens of similar age in Greenland (Van Kranendonk et al., 1993; Park, 1994; Chadwick and Garde, 1996). The Ketilidian Orogen is considered to have formed during the assembly of the supercontinent Nuna/Columbia and is correlated with the Makkovik Province in Labrador, Canada (Zhao et al., 2004; St-Onge et al., 2009; Goodenough et al., 2013), while its connection with Baltica is still unclear.

The origin of the Ketilidian orogen was first inferred as a "Himalayan type" (continent-continent) convergence by Windley (1991), but then defined as "Andean type" (ocean-continent) by Chadwick and Garde (1996). The Ketilidian orogen was formed, during ca. 130 Ma (1850-1720Ma), in response to oblique convergence between the Archean craton of Southern Greenland and an oceanic plate subducting from the South (Chadwick and Garde,

1996). At the present time neither the suture nor relics of the oceanic plate are known (Garde et al., 2002).

The Ketilidian orogen itself can be divided into four zones, following the division contained in Allaart (1975) and revised by Chadwick and Garde (1996; Figure 1):

- Border Zone: located in the north, in which the orthogneiss complex of the Archaean foreland and its local cover of Palaeoproterozoic supracrustal rocks were variably affected by Ketilidian deformation and metamorphism;
- Julianehåb batholith: previously referred to as "Granite zone", it is a zone that comprises various Ketilidian plutons and associated dykes;
- Psammite zone: previously referred to as "Fold Migmatite zone", it is a zone that comprises various pelitic and arkosic metasedimentary rocks and metavolcanics suites;
- Pelite zone: previously referred to as "Flat-lying Migmatite complex", it is a zone that comprises migmatitic paragneisses, intruded by several post-tectonic norites, monzonites and adamellites;

2.1 Border Zone

The Border Zone in the northwest of the orogen includes Ketilidian basaltic and shallow marine sedimentary rocks which rest unconformably on Archaean basement gneisses of the Vallen and Sortis group (Bondesen, 1970; Higgins, 1970). These basement gneisses are then cut by Palaeoproterozoic dolerite dyke swarms. The effects of Ketilidian deformation and metamorphism increase southward from undeformed, low-grade cover and basement into intensely deformed, high-grade supracrustal rocks and modified basement gneisses (Berthelsen & Henriksen, 1975).

The Archaean basement is cut by four generations of Palaeoproterozoic basic dykes, regarded as Iggavik suite (Berthelsen and Henriksen, 1975). Henriksen (1969) suggested that these dykes represent a period of rifting prior to Ketilidian convergence. The dykes are important indicators of increasing Ketilidian deformation and metamorphism in the basement across the Border Zone from northwest to southeast (Bondesen and Henriksen, 1965).

The cover exposed in Midternæs and Grænseland displays increasing deformation and metamorphic grade from NW to SE. The lower part of the cover, the Vallen Group (Bondesen, 1970; Higgins, 1970), overlies Archaean basement (Garde et al., 2002). The Vallen Group is overlain along a thrust by the Sortis Group, largely metabasaltic pillow lavas, pillow breccias and sills, with minor intercalations of mudstone and calcareous rocks (Bondesen, 1970). The Sortis group can represent a lateral oceanic equivalent of the Vallen Group, tectonically superimposed on the latter during early Ketilidian crustal shortening (Garde et al., 2002).

The cover on Arsuk Ø comprises metabasaltic pillow lavas and sills tectonically overlying a thin, intensely deformed succession including quartzites, phyllites, ferruginous cherts, and metagreywackes. The metasedimentary and metavolcanic rocks on Arsuk Ø are regarded, respectively, as equivalents of the Vallen and Sortis groups (Garde et al., 2002).

The Qipisarqo and Ilordleq groups constitute high-grade parts of the Ketilidian cover in the Kobberminebugt region (Berthelsen and Noe-Nygaard, 1965) and are regarded by Garde et al. (2002) as deformed screens of Vallen and Sortis group rocks trapped within intrusive members of the Julianehåb batholith.

Ketilidian metamorphism reaches upper amphibolite facies in the cover south of Kobberminebugt (Watterson, 1968; Berthelsen and Henriksen, 1975). Preliminary geochemical data from metavolcanic rocks in Midternæs, Grænseland, and Arsuk Ø point to basaltic magmatism during rifting or in an incipient back-arc at a very early stage of Ketilidian convergence. The steep ENE-trending Kobberminebugt shear zone at the approximate boundary between the Border Zone and the Julianehåb batholith coincides with the southern extreme of the basement (Garde et al., 2002).

2.2 The Julianehåb batholith

With this term, Chadwick and Garde (1996), define the polyphase granites, granodiorites, tonalites, diorites and subordinate metagabbros and amphibolite dykes which make up the wedge-shaped outcrop between the Border Zone and the Psammite Zone.

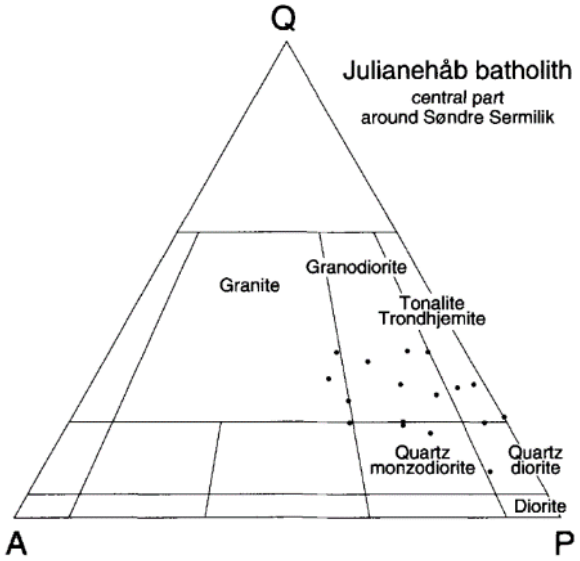

Figure 2: Composition of Julianehåb batholith (Chadwick & Garde, 1996).

The batholith widens from c. 50 km between Napasorsuaq Fjord and Kangerluluk on the east coast to c. 150 km between Kobberminebugt and Søndre Sermilik in the south-west. Its total area, including that part beneath the Inland Ice, is c. 30000 km^2 (Chadwick & Garde, 1996).

Initial Sr ratios and the absence of old U-Pb zircon ages in a suite of granitic rocks and orthogneisses in the Julianehåb batholith showed that they were juvenile additions (Van Breemen et al., 1974), not partial melts of Archaean crust as had been suggested by field evidence. The granites were regarded as partial melts of volcanic and sedimentary rocks that were older than the peak of Ketilidian metamorphism. Pb-Pb and Rb-Sr isotopic age data (Kalsbeek & Taylor, 1985; Chadwick & Garde, 1996) showed that the orthogneisses and granites were emplaced episodically within the period c. 1850-1750 Ma and the juvenile

component increases progressively southeast from the Archaean basement (Chadwick & Garde, 1996).

Chadwick et al. (1994) showed that the batholith northwest of Søndre Sermilik comprises a complex range of porphyritic granites, granodiorites, tonalites, hornblende diorites and gabbros (Figure 2) with major swarms of appinite dykes. Much of the batholith is characterized by a steeply dipping or vertical schistosity trending NE-SW. An intense linear fabric with a shallow plunge in the plane of the schistosity prevails in many outcrops.

The Søndre Sermilik area includes several steep or vertical shear zones. Many are broadly parallel to the schistosity, but others are oblique. The shear zones are mainly of two types: one, the Sârdloq shear zone, is characterized by mylonitised and ultramylonitised plutonic rocks, whereas the other, the Matorssuaq zone, is distinguished by high-strain orthogneisses (Chadwick & Garde, 1996). Hutton (1988) and Paterson et al. (1989), among others, have emphasized the critical role of linear and planar fabrics and their microtextures, in the interpretation of the tectonic setting and mechanism of emplacement of acid-intermediate plutonic rocks.

The western part of the batholith is bounded to the north by the Kobberminebugt shear zone which was described by Windley (1991) as 15 km wide, although belts of mylonite are relatively thin (c. 100 m; Harry & Oen 1964). The north coast of Napasorsuaq Fjord is dominated by undeformed granite and syenite which were intruded into fractured and mylonitised orthogneisses and metadolerite dykes (Chadwick & Garde, 1996). Comparable orthogneisses and local sillimanite-paragneisses west and north of Napasorsuaq Fjord appear to be part of the foreland in the Border Zone. The Sârdloq shear zone (Figure 1) is typical of the larger shear zones in the Julianehåb batholith.

2.3 The Psammite zone and the Pelite zone

By 1795 Ma, when the Julianehåb batholith had grown sufficiently large and stable to become uplifted and unroofed, immature erosion products from the batholith were deposited as a thick pile along the outboard, south-eastern margin of the batholith (Garde et al., 2002). Within a few million years, these sediments were deformed, metamorphosed, intruded by batholith-related magmas, and partially melted. The Psammite and Pelite zones were interpreted as the proximal parts of a fore-arc basin between the batholith and a hypothetical oceanic plate situated further south and undergoing northward subduction (Garde et al., 2002).

The Psammite zone has a sharp boundary with the Julianehåb batholith in the Søndre Sermilik area, northeast of Tasermiut and in the Sorte Nunatak area. The north-western boundary of the Psammite Zone is marked by steep NE-SW shear zones or shallow contacts with underlying granodiorite (Chadwick & Garde, 1996). The south-eastern boundary of the Psammite Zone on the west coast is arbitrary because of the abundance of plutons of the Ilua plutonic suite (previously referred to as “rapakivi granites”, Chadwick & Garde, 1996; Steenfelt et al., 2016). The south-eastern boundary on the east coast is a transition zone south of Lindenow Fjord, where intensely migmatized pelites with relatively shallow dips become predominant over psammites.

In the northeast of the peninsula between Søndre Sermilik and Tasermiut (Figure 1) the supracrustal rocks of the Psammite Zone lie within a large-scale asymmetrical syncline at right angles to the trend of the Julianehåb batholith.

Strongly foliated, partly migmatized semi-pelites which immediately overlie the batholith are followed by c. 500 m of schistose amphibolites with local pillow structures and breccias with deformed fragments of leucogabbro and mafic amphibolite (Chadwick & Garde, 1996). The amphibolites are overlain by a thin layer of black pelites and c. 1000 m of psammites. The psammites in the shallow limb are intensely migmatized, but those in the steep overturned limb are less migmatized and preserve through cross-bedding and grading which show that the stratigraphy is right way up (Chadwick & Garde, 1996).

Coarse polymict conglomerates with well-rounded clasts of granodiorite and smaller clasts of metavolcanic rocks, vein quartz, metadolerite and a variety of granitic compositions, are interbedded with the psammites (Chadwick & Garde, 1996). The rounding of the clasts and the common trough cross-bedding indicate a high energy fluvial or marine deltaic environment.

There are no unambiguous field indications of the age of the basement to the metasedimentary and metavolcanic rocks of the Psammite Zone, although three lines of circumstantial evidence, defined by Chadwick and Garde (1996), point to the Julianehåb batholith as the basement and provenance:

- The abundance of alkali feldspar in the psammites and the common clasts of granite in the conglomerates indicate a granitic provenance not far removed from the sedimentary basin. The rounding of the clasts suggests either a fluvial or shallow marine environment or a two-stage depositional process in which rivers delivered rounded clasts to the basin margin before they were reworked in marine environments. The abundance of detrital titanite, apatite, zircon and magnetite in the psammites is also consistent with a provenance of granitic and dioritic rocks similar to those in the Julianehåb batholith. The mainly tonalitic composition and distance from the basin make the gneisses of the Archaean foreland an unlikely source of detrital alkali feldspar and boulders of granite.
- The second thread of circumstantial evidence comes from relationships between the supracrustal rocks and the underlying batholith in Sorte Nunatak and south of Søndre Sermilik. The contacts in the Sorte Nunatak area may be interpreted both as unconformable and intrusive, but the presence of granitic clasts in the conglomerates strongly suggests that the Julianehåb batholith was the basement and provenance. The contact between the granodiorites and the overlying supracrustal rocks southeast of Søndre Sermilik suggests age relationships comparable to those in Sorte Nunatak, although sheared areas seen from the air may be the result of thrusting.
- The third line of evidence is the general absence of xenoliths of supracrustal rocks in the batholith, apart from certain large bodies of pale quartzo-feldspathic rocks (Chadwick et al., 1994) in the granites west of Søndre Sermilik and minor occurrences of cordierite-andalusite gneisses to the north which were interpreted as metasedimentary rocks by Persoz (1969).

The Pelite Zone (Figure 1) comprises mainly flat-lying, intensely migmatized pelitic rocks. Relics of psammites, some with cross-bedding, occur as thin, boudinaged resistor layers or as xenoliths in the lenses of anatectic granite and the sheets of Ilua plutonic suite's granites (Chadwick & Garde, 1996).

2.4 Deformation history and geodynamic setting in the Psammite and Pelite zone

Four episodes of deformation, D_1-D_4, and a localised phase, D_5, have been recognised in the Ketilidian fore arc (Garde et al. 2002). Much of the fore-arc deformation happened during the first three phases (D_1-D_3) and resulted from sinistral transpression, prevailing during the earlier construction of the Julianehåb batholith. The later stages of the deformation instead (D_4-D_5) and the emplacement of the rapakivi suite took place long after the batholith emplacement had ceased. D_1-D_3 phases were accompanied by regional High-Temperature, Low-Pressure (HT-LP) metamorphism, widespread anatexis and emplacement of batholith related felsic to mafic intrusions and major flat lying sheet of s-type granite besides thin and numerous intermediate to ultrabasic appinite dykes and sills (Garde et al. 2002).

Radiometric ages of syn-D_2 batholith-related intrusions and syn-D_3 S-type granites show that D_1–D_3 deformation and partial melting took place in a short interval, ca. 1792–1785 Ma (Hamilton et al., 1996), whereas the latest deformation, D_4–D_5, was contemporaneous with intrusion of the Ilua plutonic suite (Chadwick et al., 2000).

The two earliest phases of deformation (D_1-D_2) in the Psammite Zone were essentially coaxial and coplanar and gave rise to generally flat-lying structures with intense composite S_1–S_2 LS fabrics and tight to isoclinal folds (Chadwick et al. 1997; Garde et al. 1997).

In inner Danell Fjord, the contact between the batholith and the fore arc is a steep, northeast-trending sinistral ductile shear zone, which is correlated with the sinistral transpressive system of the Julianehåb batholith (Garde et al., 2002). From here the metamorphic grade and intensity of D_2 deformation increase eastwards: bedding and S_1 are transposed to a composite D_1–D_2 LS fabric with a marked northeast-trending extension lineation, and D_1 migmatite seams arising from differential anatexis of S_1 layering are folded by F_2 folds. New migmatite seams parallel to F_2 axial surfaces show that the high-grade conditions with partial melting persisted into D_2 (Garde et al., 2002). In the southwestern Psammite Zone (Escher, 1966; Wallis, 1966; Higgins et al., 1970), the composite D_1–D_2 structures have the same flat-lying orientation as at central Danell Fjord (Garde et al., 2002).

The tectonic evolution during D_1–D_3 was accompanied by HT–LP metamorphism including extensive partial melting in the Psammite and Pelite Zones (Garde et al., 2002). Garde et al. (1998) presented preliminary pressure-temperature (P–T) determinations of garnet–biotite–sillimanite ± cordierite-bearing parageneses in schists from most of the fore arc. From their study the peak metamorphism was defined at 3 kbar, 580°C at the batholith margin in inner Danell Fjord increasing to 5 kbar, > 800°C south of Prins Christian Sund.

The metamorphic peak predated the earliest members of the Ilua plutonic suite by at least 30 Ma and occurred during the main D_1–D_3 deformation (Garde et al., 2002).

The presence of a HT-LP metamorphism in a contractional tectonic environment is unusual, accounting for the heat source are I-type magmas, such as the Stendalen complex and sheets of diorite and granite, which intruded the supracrustal pile during the D_1-D_2 deformation, likely contributing to some of the heat (Garde et al., 2002). Mafic underplating has also been suggested as a possible heat source and the numerous appinite dykes present in the entire fore arc may support this hypothesis (Dempster et al., 1991; Chadwick & Garde, 1996).

D_4 deformation is most widely developed in the outer part of the fore arc. F_4 folds are kilometre-scale and open to tight, with upright axial surfaces trending mainly northeast with shallow northeast plunge. F_4 folds appear to postdate the peak of metamorphism because they are only rarely associated with penetrative fabrics, and large S-type and I-type granites are folded by F_4 folds (Garde et al., 2002).

Irregular granitic dykes commingled with hornblende diorite or crowded with ultrabasic xenoliths may have been emplaced during D_4. A few undeformed appinite dykes occur parallel to F_4 axial surfaces (Garde et al., 2002). F_5 folds have instead a much more restricted distribution. They are relatively open, large-scale warps with variable trend and locally interfere with F_4 folds to form open dome- or basin-like folds (Garde et al., 2002).

2.5 Local geology of the Amitsoq area – Nanortalik Nappe

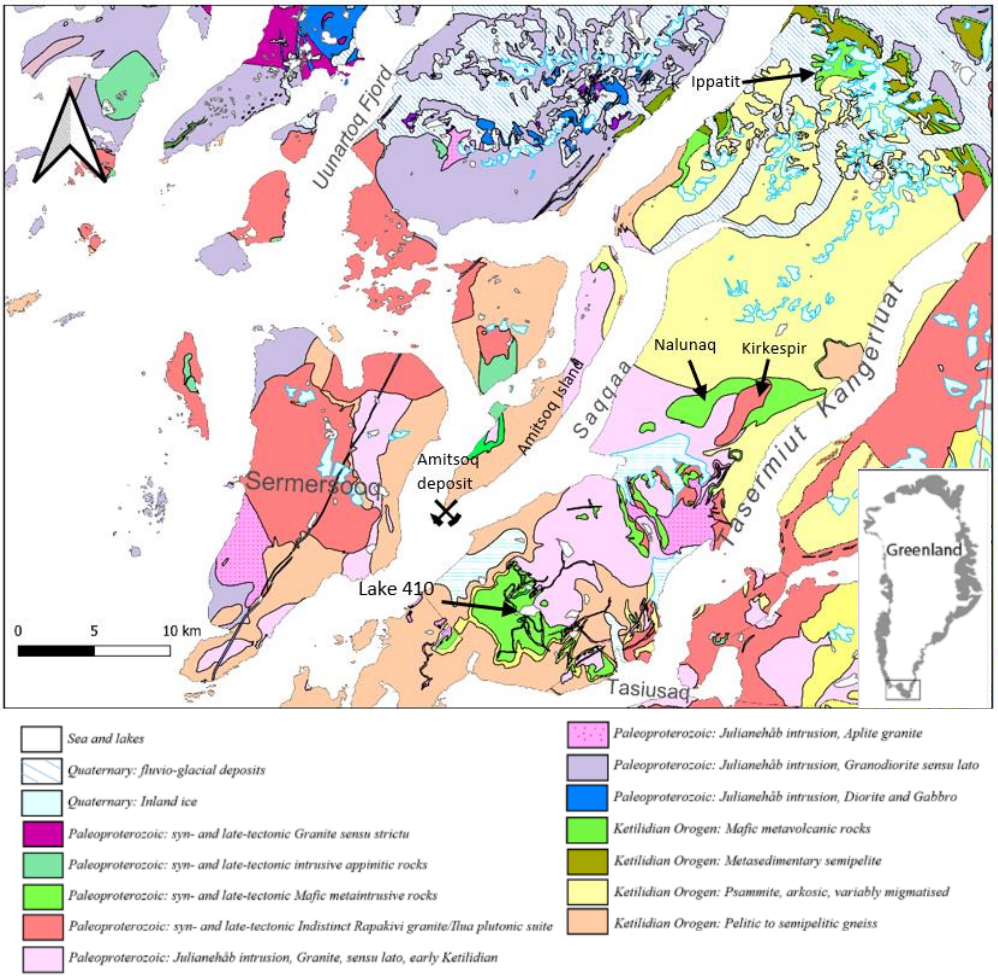

Figure 3: Geological map of the Nanortalik Nappe (from geus.dk).

The Amitsoq graphite deposit is located on the southernmost tip of the Amitsoq Island and is located in the Psammite zone of the Ketilidian orogen. The Island is composed of pelitic to semi-pelitic gneisses in amphibolite facies, locally migmatized, by metamorphosed granites from the Julianehåb pluton and later basic intrusions (Allaart, 1975).

The gneisses are part of the Nanortalik Nappe, which is a term used to describe a sequence of meta-sedimentary rocks, banded quartz-graphite-sulphide rocks and variably metamorphosed mafic volcanic rocks that are thrust over the meta-sedimentary rocks (Petersen et al., 1997; Kaltoft et al., 2000).

Escher (1966) recognized five principal units of supracrustal rocks in the Nanortalik peninsula in the extreme southwest of the Psammite Zone. They are dominated by variably migmatized pelites, semi-pelites, psammites and metavolcanic amphibolites with local pillow structures and agglomerates (Figure 3; Chadwick & Garde, 1996). Four hornblende peridotite dyke-like intrusions presumably belonging to the Ilua plutonic suite (Berrangé, 1970; Schønwandt 1971; Secher and Stendal, 2010) are known from either side of Sermilik and on the island north of the Amitsoq graphite mine.

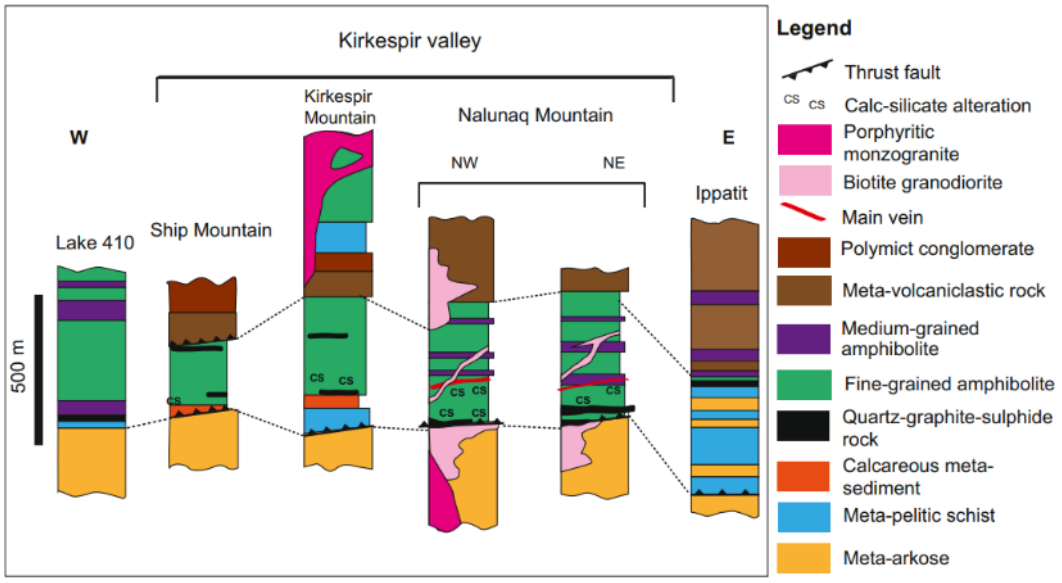

Figure 4 stratigraphic sequences for sections of the Nanortalik Nappe, the term "Main Vein" refers to a gold mineralisation in Nalunaq (from Bell et al., 2017).

In the Nanortalik nappe there are several occurrences of what is referred to as "bands of 2–8-m-wide banded quartz-graphite-sulphide rocks" (Figure 4; Bell et al., 2017) that form an important marker horizon in the area, although is unclear whether these levels are what is considered the ore body on the Amitsoq Island.

At Amitsoq, graphitic schist occurs in cordierite–sillimanite–biotite gneiss. The ore on the Amitsoq Island occurs in a zone that is c. 1 km long and up to 50 m wide. For most of its length, two WNW-dipping layers occur in this zone, but they vary in thickness, mainly between 0-4 m, but cumulating in a width of 16.5 m where the old mine is located. The ore consists of finely disseminated crystalline graphite flakes in a quartz-rich groundmass, accompanied by minor pyrite and biotite. The graphite flakes are up to 15 mm in size and the graphite content varies between 20 and 24 vol.% (Ball, 1923; Bondam, 1992).

Close to the Amitsoq deposit, in the Nalunaq mountain, four deformation stages were identified:

- The first stage (D_1) is recognized by moderately SE-dipping foliation (S_1) in the meta-volcanic rocks, with metabasalts and metadolerites metamorphosed to amphibolite facies (Kaltoft et al. 2000; Bell et al., 2017). Metamorphism is accompanied by a weak S_1 foliation, correlated to D_1 which is dated at > 1792 Ma
- Development of large reverse-sense shear zones documented as dipping at 45° SE (D_2), slightly oblique to S_1, which developed in the brittle–ductile regime under lower amphibolite–upper greenschist facies metamorphic conditions (Bell et al., 2018). The D_2 deformation stage is associated with regional HT-LP metamorphism in the Southern Domain with numerous granitic intrusions formed between ca. 1795 and 1785 Ma (Garde et al., 2002)
- The third stage (D_3) is characterized by normal reactivation of the shear zones, with local vertical extension in the upper greenschist facies (Bell et al., 2018)
- The Ilua Plutonic Suite intruded contemporaneously with late-stage fault development (D_4) (Bell et al., 2017).

2.6 Ilua plutonic suite

Melting of both mantle and crust took place late in the Ketilidian evolution and produced a plutonic suite that was emplaced primarily in the Southern Domain. The plutonic rocks cover ca. 3000 km^2 in total and they were emplaced from c. 1755 to 1723 Ma mainly as extensive flat-lying sheets into the supracrustal rocks that also occur as xenoliths in the plutonic rocks (Grocott et al., 1999; Garde et al., 2002).

The suite comprises norite, syenite, monzonite and quartz monzonite to granodiorite and granite (Brown et al., 1992, 1999; Harrison et al., 1990; Grocott et al., 1999; Chadwick et al., 2000). A geochemical signature with high P, Ti, Ga, Y, Hf, Zr and elevated Zn and REE for the granitic plutons (Brown et al., 1992, 1999; Steenfelt et al., 2005) suggests they belong to A-type granites derived by deep crustal melting, while the norites probably result from mantle melting (Patchett and Bridgwater, 1984; Harrison et al., 1990; Brown et al., 1999). Most authors agree that underplating of mafic magmas was the reason for the melting of lithospheric mantle and deep crust that resulted in the Ilua plutonic suite emplaced at high crustal level, but controversy exists about the geotectonic setting and emplacement mechanism of the magmas (Steenfelt et al., 2016).

Four hornblende peridotite dyke-like intrusions presumably belonging to the Ilua plutonic suite (Berrangé, 1970; Schønwandt 1971; Secher and Stendal, 2010) are known from either side of Sermilik and on the island north of the Amitsoq graphite mine.

3. Methods

3.1 Optical Microscopy

Petrography has been carried out both at University of Copenhagen with a Leica DM4 P microscope in transmitted and reflected light and at Alma Mater Studiorum University of Bologna with a Zeiss AxioScope 7 microscope in transmitted and reflected light. Both microscopes were equipped with cameras. The petrography study is based on a set of eleven thin sections from the ore body, twenty-four from the inferred host rock, two thin sections from the Ilua Plutonic Suite and one thin section from the Julianehåb igneous complex.

3.2 EPMA

Silicate minerals from the ore body and from the country rock were analyzed with a JEOL JXA-8200 Superprobe at the University of Copenhagen. The analyses were performed at probe current = 15 nA, accelerating voltage = 15kV and spot size of 5µm. Counting time was 10-20 seconds on peak and background. The instrument was standardised regularly before measurements. The silicate minerals were analyzed for the major elements SiO_2, FeO, K_2O, NiO, Na_2O, Al_2O_3, MnO, CaO, Cr_2O_3, MgO, and TiO_2. Four thin sections from the ore and six from the country rock were analyzed. Prior to the analyses, all the thin sections were carbon coated and placed a sample holder with the addition of carbon tape (Figure 5)

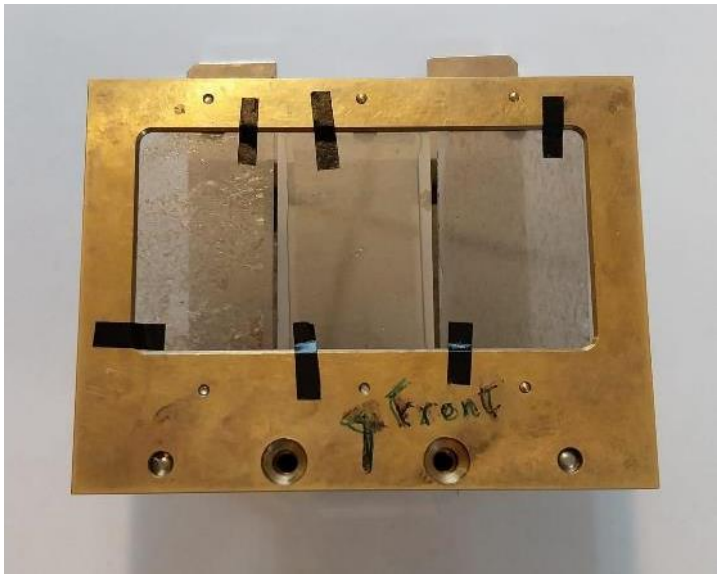

Figure 5: example of coated thin sections with carbon tape on the sample holder of the microprobe at University of Copenhagen.

3.3 X-Ray fluorescence scanning (µ-XRF)

A Bruker Tornado M4+ at University of Copenhagen was used to generate element maps, which were then used to further help identifying targets for the microprobe and to obtain quantitative data from thin section scanning and quarter core scanning. The analyses were performed with Rh tube, with 50 kV of high voltage and 600 µA anode current at 1.3 mbar pressure in the chamber. Measurement spot size of 20 µm, with 20 ms/pixel dwell time. This kind of instrument does not require any sample preparation other than placing the thin

sections/rock pieces on the sample holder with the surface perpendicular to the incident beam (Figure 6).

Figure 6: thin sections on the sample holder of μ-XRF

3.4 X-Ray Diffraction (XRD)

Three different hand samples were selected and cut (Figure 7A) to prepare 15-gram aliquots for each sample. The rock pieces were hammered and then separately milled in a Retsch PM100 mill at 460 rpm for 1.5 minutes (Figure 7B-C).

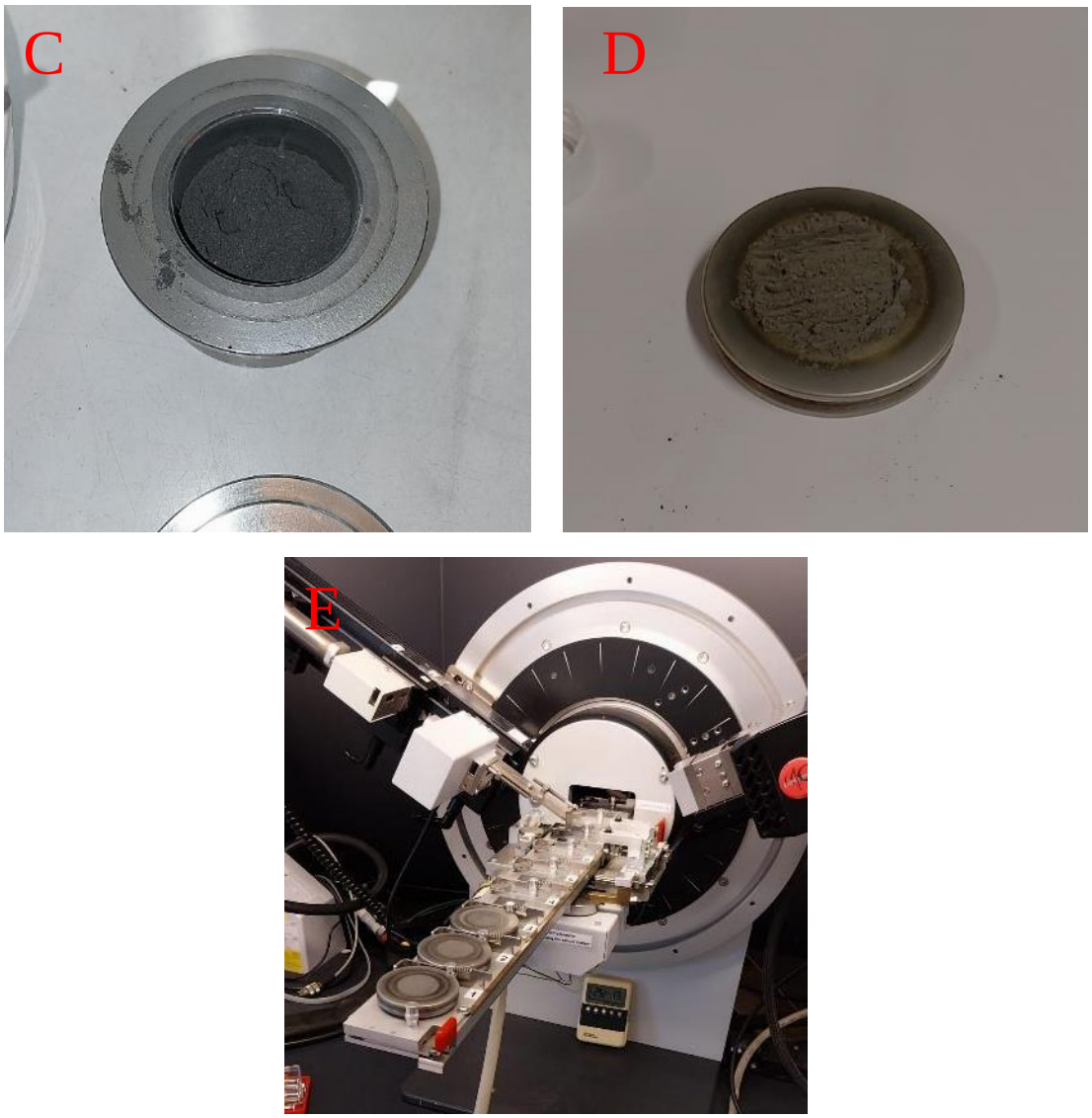

Figure 7: Several steps in the sample preparation and analysis for XRD. A: the samples were cut to have clean surfaces and reach approximately 15g. B: Steel balls of the ball mill. C: Grounded powder after milling. D: Powder on the sample holder. E: Samples inside the XRD.

The powder thus created was placed on XRD sample holders trying to minimize the effect of iso-orientation of crystals (Figure 7D) and then was run from 5-90 degrees with a step size of 0.02 degrees, measuring 4 seconds per step. The analysis was carried using a Bruker-AXS D8 Advance diffractometer at University of Copenhagen (Figure 7E). This diffractometer is equipped with a Cu X-ray tube (λ = 1.5406 Å), a primary beam Ge111 monochromator and a silicon-strip LynxEye detector with a 3.3° opening. The qualitative analyses were performed using the Bruker DIFFRAC.EVA software. The quantitative analyses were performed using the Rietveld refinement method and the Bruker DIFFRAC.TOPAS version6 software.

3.5 Raman Spectroscopy

MicroRaman spectroscopy was used to analyse solid and fluid inclusions from three thin sections, one from the ore and two from the supposed host rock. The analyses were carried out on a WITec Alpha 300 MicroRaman at the Department of Biological, Geological, and Environmental Sciences, Bologna University, Italy. The facility is equipped with a 532 nm

green laser. The laser power reaching the sample, as measured by the WITec TruePower system, 32 mW for fluid inclusions, and 2.5 mW for graphite. Five acquisitions of 60s were set for graphite analyses, whereas ten acquisitions and 60s were set for fluid inclusion analysis. Grating was set at 600 grooves/mm.

3.6 $\delta^{13}C$ and $\delta^{34}S$

Stable carbon isotope analyses were performed at St. Andrew University by Dr. Eva Stueeken on nine samples from the ore body. The samples were hammered into mm-sized chips with a steel pestle on a steel plate and then pulverized in an agate ball mill for 15 minutes. The mill was cleaned with pre-combusted (500 °C overnight) silica sand and wiped with DI-water (18 MOhm/cm) and methanol (reagent grade) in between samples. The powders were stored in pre-combusted scintillation vials. Prior to analysis, a 0.5g aliquot of each sample powder was decarbonated with 10ml 2N HCl in pre-combusted glass centrifuge tubes. The acid was left to react at 70 °C overnight in an acid-proof oven. The next day, the samples were centrifuged (700 rpm for 15 minutes) and the acid was decanted. The residual powder was washed three times with DI-water and then left to dry in the oven for two days. For analysis, 0.15mg of each sample were weighed into tin capsules and analysed for carbon isotopes by flash combustion with an EA-Isolink, coupled to a MAT253 IRMS via a Conflo IV. The measurements were calibrated to the delta scale with the international reference materials USGS-40 and USGS-41. Abundances were calibrated with peak areas. Aliquots of USGS-24 (graphite), USGS-62 (caffeine) and SDo-1 (shale, decarbonated) were analysed within the same run for quality control.
The graphite samples prior to the $\delta^{34}S$ analysis were ashed at 850 °C for 24 hours.

4. Results

4.1 Petrography

The petrography study is based on a set of eleven thin sections from the ore body, twenty-four from the inferred host rock, one from the Julianehåb igneous complex, and three from the Ilua Plutonic Suite. The thin sections are sourced from various locations across a wide area, and their respective positions are indicated in Figure 8.

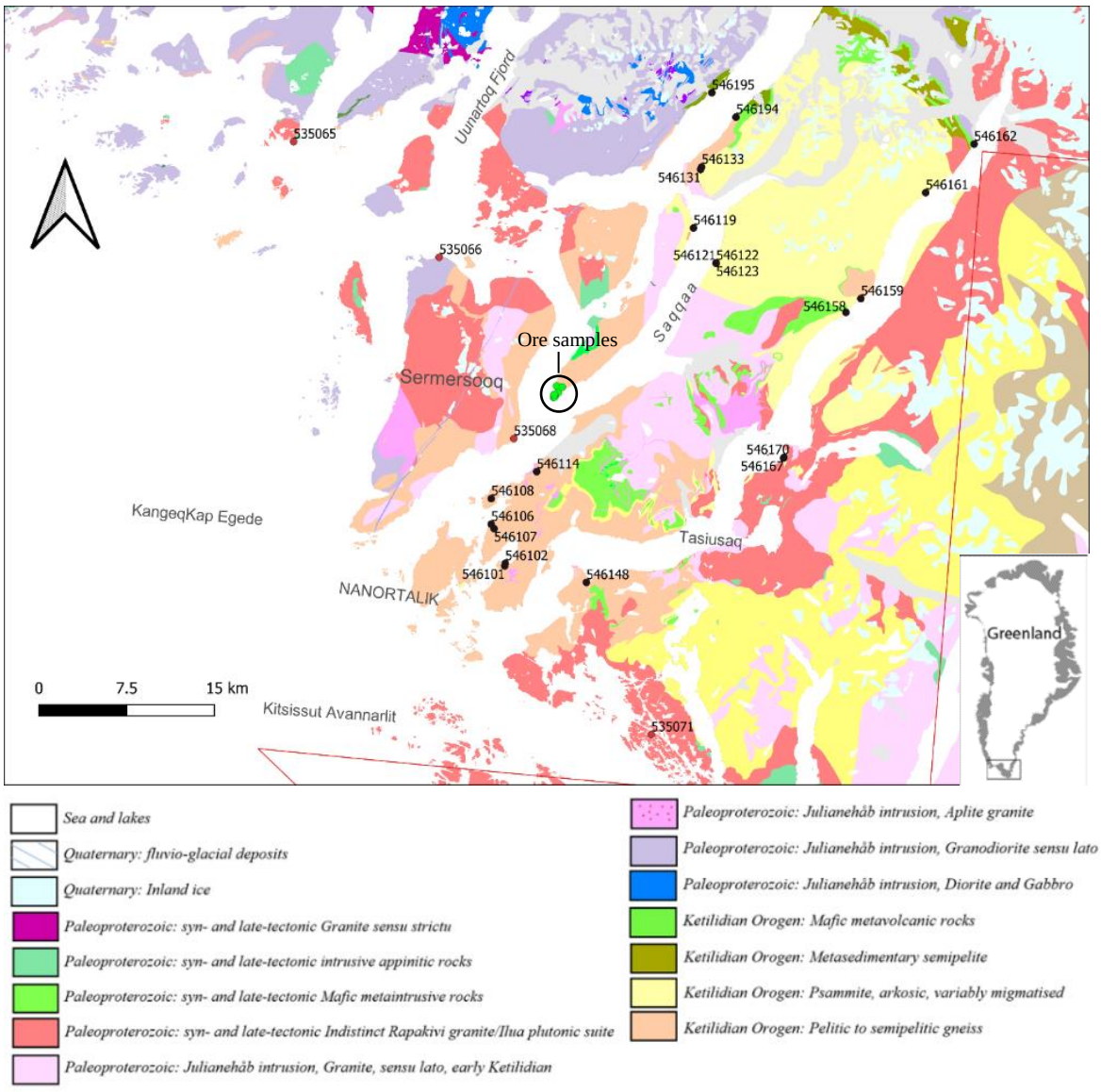

Figure 8: position of studied thin sections.

List of samples			
535065	Julianehåb	546123	Meta psammite
535066	Ilua plutonic suite	546131	Meta psammite
535068	Pelitic gneiss	546148	Pelitic gneiss
535071	Ilua plutonic suite	546158	Meta psammite
546101	Pelitic gneiss	546159	Meta psammite
546102	Pelitic gneiss	546161	Meta psammite
546106	Pelitic gneiss	546162	Meta sedimentary semipelite
546107	Pelitic gneiss	546167	Meta psammite
546108	Pelitic gneiss	546168	Meta psammite
546114	Pelitic gneiss	546170	Meta psammite
546119	Meta psammite	546194	Pelitic gneiss
546121	Meta psammite	546195	Metasedimentary semipelite
546122	Meta psammite	●	Ore samples

Table 1: list of samples.

4.1.1 Ilua plutonic suite

The samples analyzed from the Ilua Plutonic Suite are dominated by feldspars and quartz, comprising 80 to 85% of the thin sections. Quartz is present in two forms: rounded crystals (Figure 9A) surrounded by feldspars, and anhedral crystals. The remaining mineral assemblage consists of micas, likely biotite and muscovite, and amphiboles. The amphiboles form rims around the mica (Figure 9B), and these minerals are irregularly distributed. Quartz and feldspar crystals tend to be coarser than the mafic minerals. The sample shows extensive alteration, with significant sericitic alteration observed on the feldspars (Figure 9C) and altered mica crystals (Figure 9D).

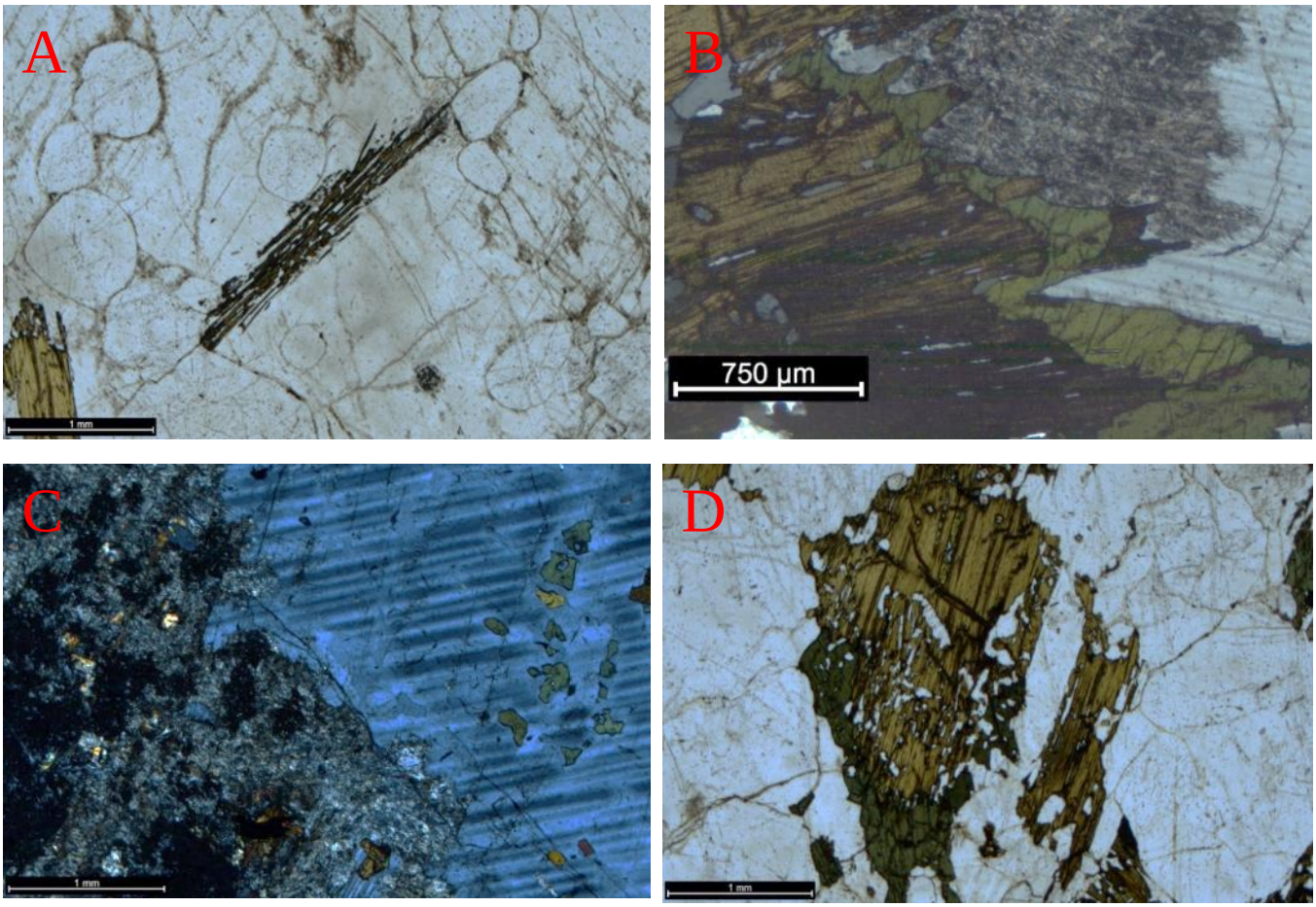

Figure 9: A: Altered mica in quartzo-feldspathic matrix, roundish quartz around. B: Amphibole rimming mica crystal. C: Polysynthetic twinning of plagioclase with sericitic alteration. D: Altered mica surrounded by feldspar crystals.

Figure 10 (Next page): Altered hornblende with characteristic 56°-124° cleavages and oxide in the centre of the crystal; B: mica crystals growing around quartz; C: Consumed amphibole; D: Sericitic alteration of perthitic feldspar; E: Feldspar consuming amphibole; F: Anhedral assemblage of mica and amphibole.

4.1.2 Julianehåb batholith

The sample from the Julianehåb complex can be classified as Hbl-Bt-granodiorite, with mafic minerals comprising up to 20% of the total composition. The thin sections exhibit abundant quartz and plagioclase, as expected in plutonic bodies of this nature, along with a significant presence of amphibole and mica. Amphibole is widely distributed, appearing either as euhedral crystals with distinct and well-defined cleavages ranging from 56° to 124° (Figure 10A) or as corroded crystals (Figure 10B). Micas are also present, mostly in anhedral form, with a few examples showing growth around feldspar crystals (Figure 10C). Overall, the mineral assemblage exhibits alteration textures, such as sericitic alteration observed in plagioclase (Figure 10D), as well as altered amphibole and mica (Figure 10E-F).

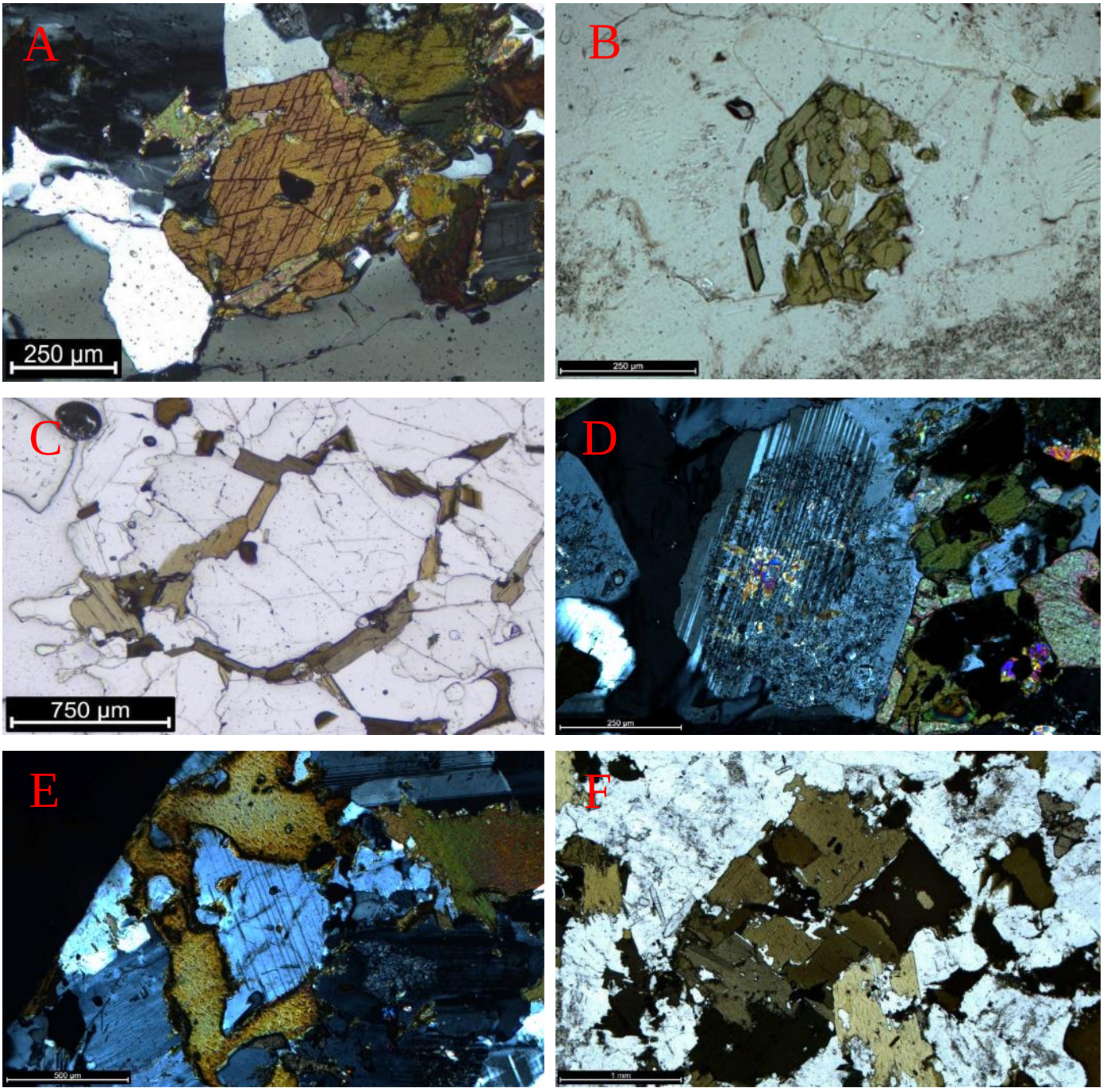

4.1.3 Host rock - Meta-psammite/semipelitic gneiss

The samples are gneisses that exhibit a diverse mineralogical composition and various textural patterns. The primary constituents include quartz, feldspars, biotite (which defines the main foliation of the rock), and amphiboles. In a few thin sections, the presence of sillimanite was observed (Figure 11A). Thin sections 546114 and 546194 displayed a graphite content similar to that observed in the ore at Amitsoq. It is worth mentioning that graphite flakes are frequently interleaved with biotite. Biotite appears in two distinct textural forms: as discrete single crystals and as intertwined plait-like aggregates (Figure 11B). The amphiboles identified in the thin sections and analyzed by EPMA predominantly consist of low-Ca species, namely anthophyllite and ferrogedrite.

Additionally, two thin sections, 546102 and 546168, exhibited the presence of garnet. The first thin section displayed poikiloblastic garnet occurring in contact with feldspars and biotite (Figure 11C). The other thin section showed garnet with clinopyroxene crystals included within the garnet crystal (Figure 11D).

Textural variations are apparent, ranging from a fine-grained matrix to an equigranular assemblage of minerals. Folding and variable grain sizes are observed. Samples that are geographically closer to the ore exhibit the same schistosity, defined by biotite crystals and alternating coarse and finer domains (Figure 11E). A noteworthy finding in some of the examined thin sections is the presence of accessory graphite, characterized by a flaky morphology and often interleaved with biotite (Figure 11F).

Furthermore, several thin sections show the presence of minor mineral phases such as Ti-oxides, Fe-sulphides, and La-Ce-Monazite.

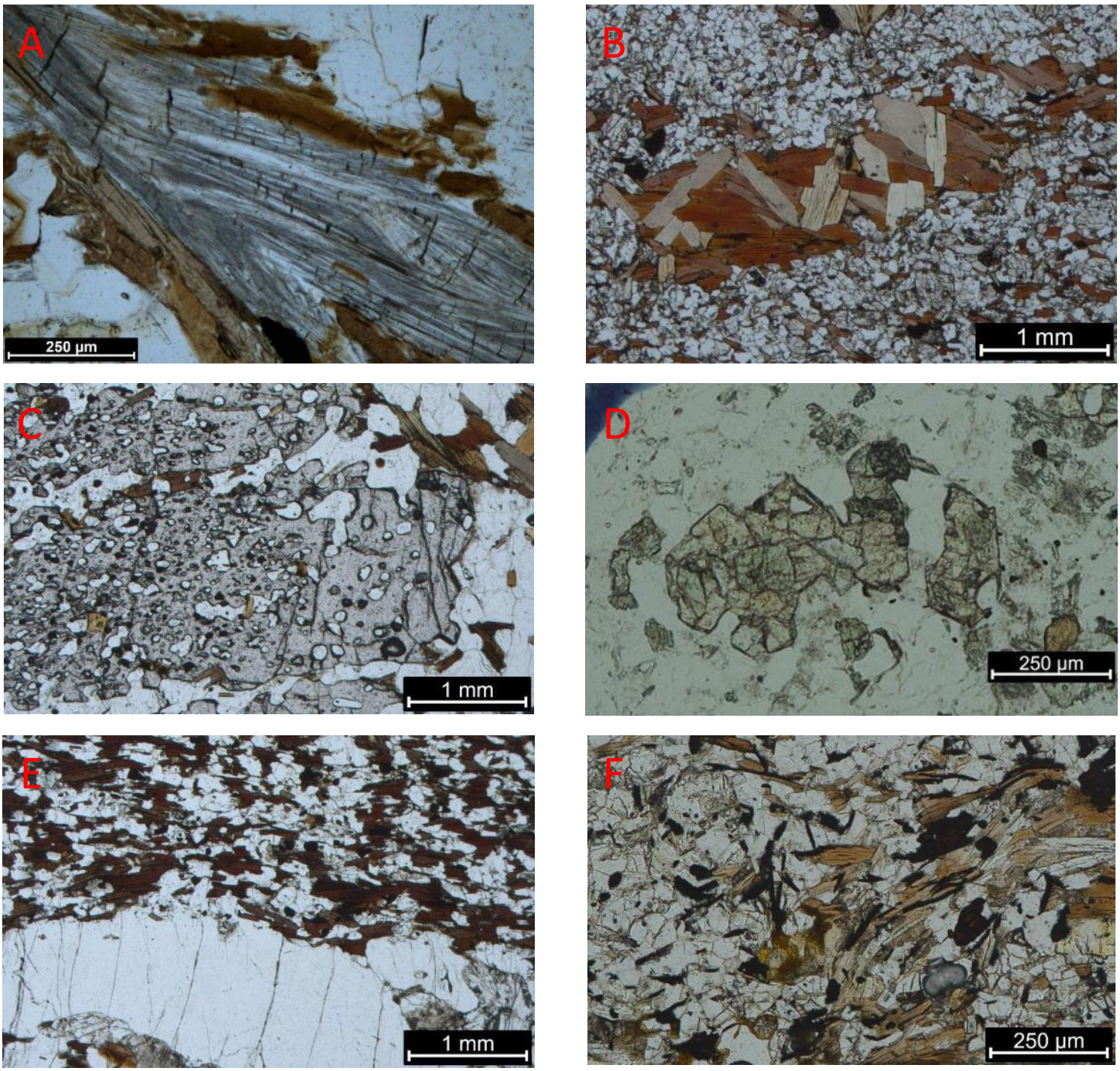

Figure 11: A: Fibrous sillimanite surrounded by biotite; B: plait-like biotite; C: Poikiloblastic garnet; D: different domains, coarse one quartz-dominated and finer one, biotite rich; E: Round hedenbergite in garnet crystal; F: example of graphite flake interleaved with biotite.

Fluid inclusions

Some of the analyzed thin sections of the host rock displayed trails of fluid inclusions, primarily characterized by irregular shapes. These fluid inclusions exhibited both liquid and gaseous phases, with the liquid phase being dominant. The Raman spectroscopy analysis of the fluid inclusion shown in Figure 12 will be presented in Chapter 4.5.

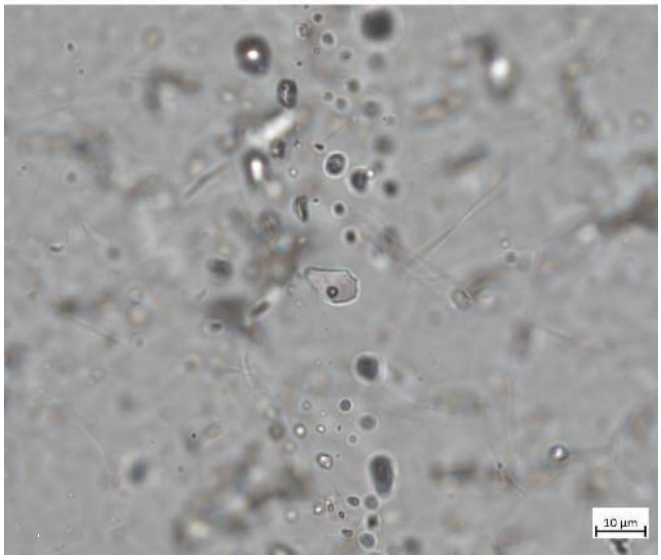

Figure 12: trails of fluid inclusion from the host rock.

4.1.4 Ore body – Amitsoq graphite deposit

The rock that hosts graphite at Amitsoq is a heterogeneous graphitic-sulphidic quartzo-feldspathic schist. This rock type is composed of graphite, pyrrhotite, quartz, and variable amounts of biotite and feldspars. The foliation is defined by graphite flakes, biotite, and by layering in mineralogy and grain size distribution. In coarse-grained domains, the dominant minerals are quartz and graphite, and depending on the thin section. Graphite is observed in two main habitus: a crypto-crystalline one with very small grain size and a flaky habit with millimetre-sized flakes (Figure 13A), which can also occur as stacks of graphite (Figure 13B). The larger flakes are often interleaved with pyrrhotite and/or biotite (Figure 13C-D). All the analyzed thin sections exhibit varying degrees of deformation, with different styles, including tight folding of graphite (Figure 13E), pinch and swell structures with quartz and graphite (Figure 13F), and sinistral sigmoids. At least two folding phases can be discerned from the thin sections, resulting in a complex intersection pattern. During folding, mineral recrystallization occurred, causing more competent minerals (including quartz and pyrrhotite) to concentrate in the fold hinges, while micas and graphite became more abundant in the fold flanks. Generally, the grain size is coarser in the fold hinges compared to the flanks.

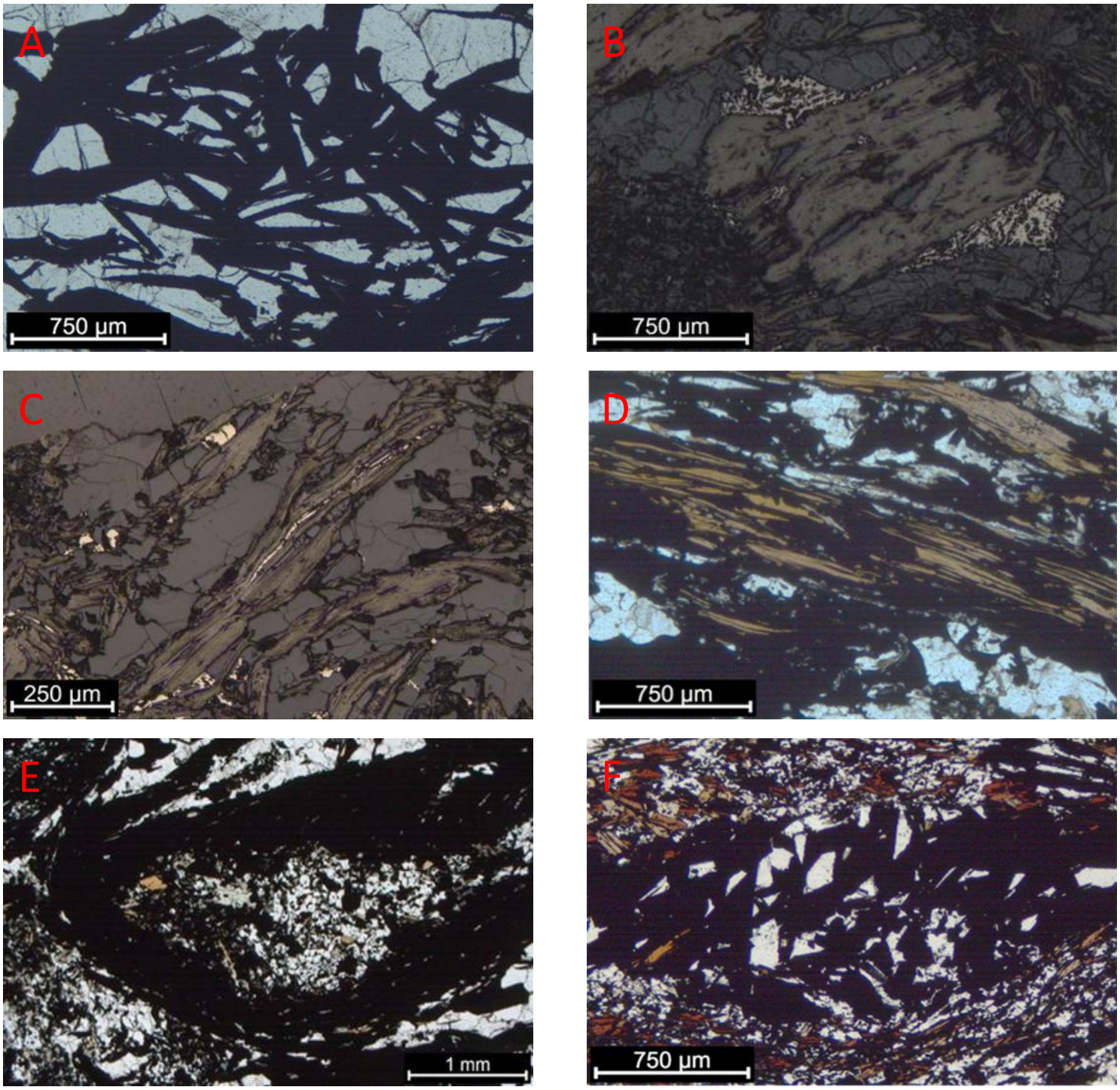

Figure 13 A: Randomly oriented millimetric graphite flakes Graphite interleaved with pyrrhotite; B: Stack of graphite; C: Graphite interleaved with pyrrhotite; D: Biotite interleaved with graphite; E: Tight folded graphite. F: Swell of graphite and quartz in a pinch and swell structure.

The observation in back-scattered electrons, done with electron microprobe, allowed the identification of accessory minerals, which include sphalerite, apatite, and minor of uraninite and monazite (Figure 14).

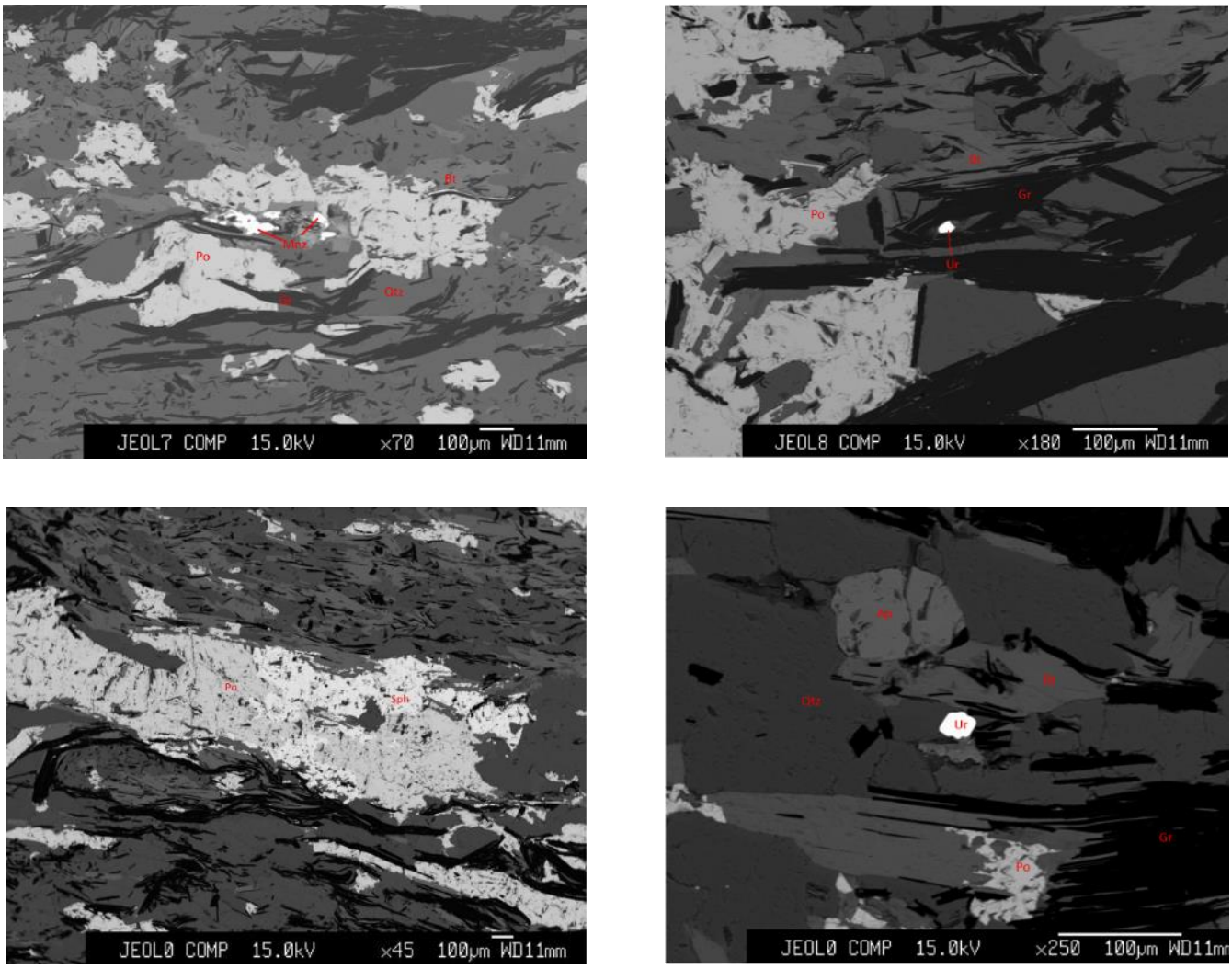

Figure 14: Back-scattered electrons images of thin sections from the ore. Abbreviations: Ap: apatite; Bt: biotite; Gr: graphite; Mnz: monazite; Po: pyrrhotite; Qtz: quartz; Sph: sphalerite; Ur: uraninite.

Fluid inclusions

In some thin sections of the ore, coarse quartz veins contain trails of fluid inclusions. Most of these trails seem to be propagating from the edges of graphite flakes (Figure 15). Fluid inclusions occur in different shapes, they can be square-shaped, irregular, or elongated. Raman spectroscopy of a fluid inclusion present in Figure 15 will be shown in chapter 4.5.

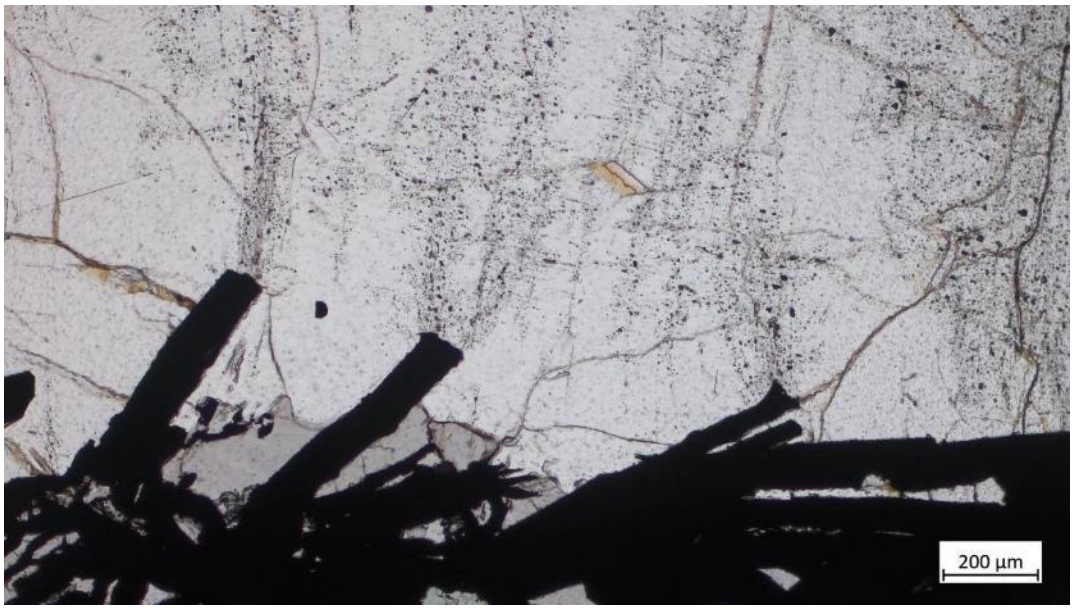

Figure 15: trails of fluid inclusion propagating from graphite flakes.

4.2 EMPA

Microprobe analysis yielded the detailed composition of selected mineral phases in the ore body and host rock.

4.2.1 Feldspars

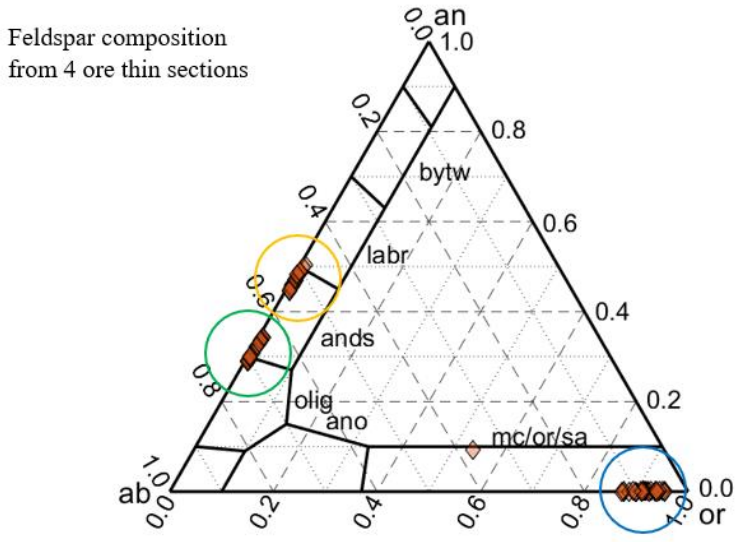

Figure 16 Ternary diagram showing feldspar composition of the ore.

Feldspar composition of the ore body lies in the clusters showed in Figure 16. It is important to specify that the three clusters refer to three different thin sections and that only in the case of the fourth one there is an overlap with the blue and green zones. The feldspars in the ore body show no compositional variations between cores and rims.

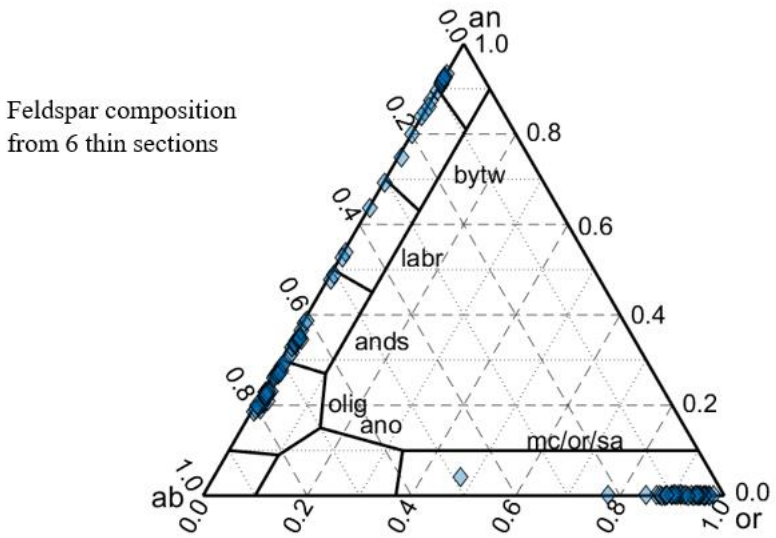

Figure 17: Ternary diagram showing feldspar composition of the host.

Host rock feldspar composition (Figure 17) is more spread on the plagioclase line of the ternary diagram, 5 out of 6 thin sections show bimodal feldspar composition but without compositional variations between cores and rims of single crystal.

4.2.2 Micas

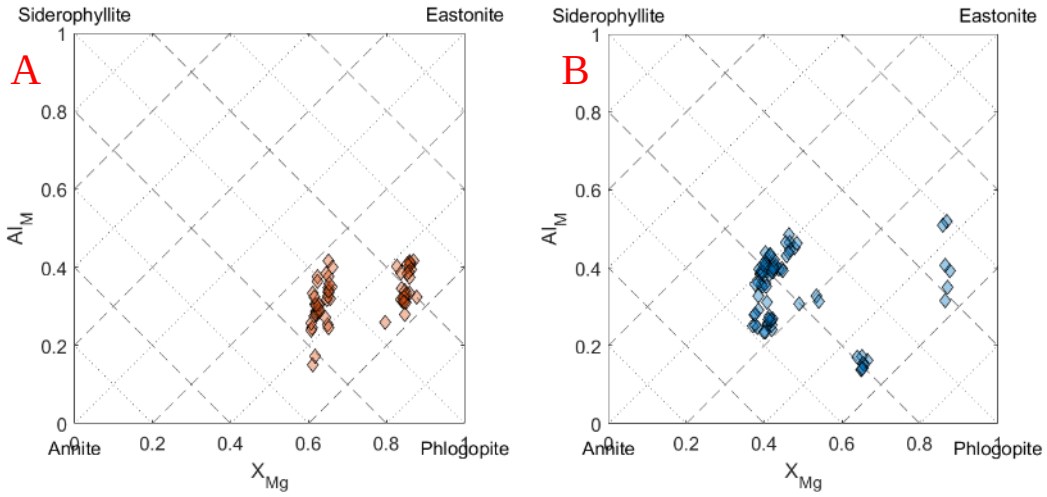

Figure 18: Mica composition from the ore (A) and from the host (B).

In Figure 18 composition of mica crystals from the ore (A) and the host (B) are plotted on octahedral mica plot.

4.2.3 Garnets

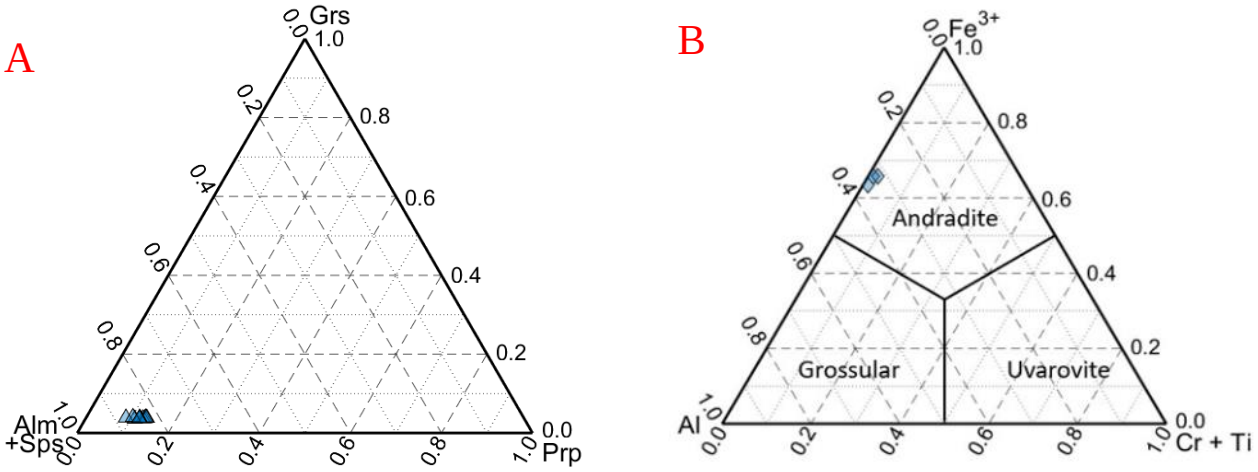

Figure 19: Garnet composition of thin section 546102 (A) and 546167 (B) form di hostrock.

Garnet was identified in only two samples of the host rock, each of which only shows almost pure endmember composition of garnet on the ternary diagram, with sample 546102 showing almost pure almandine + spessartine composition (Figure 19A) and sample 546168 showing andradite composition (Figure 19B).

4.2.4 Pyroxenes

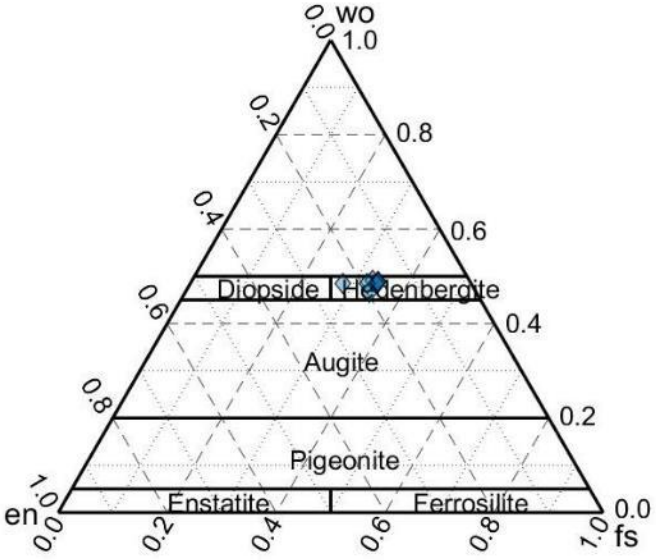

Figure 20: Pyroxene composition from thin section 546167.

Among the analysed thin sections, pyroxenes were recognised and analysed only in one thin section from the host rock, all the pyroxenes that were analysed were identified as hedenbergite crystals (Figure 20).

4.3 Micro-X-Ray Fluorescence (μ-XRF)

Outcome of this analyses were detailed chemical maps showing the element distribution in the thin sections of the ore. Here I report as an example two chemical maps (Figure 21) from the ore with light blue colour highlighting the presence of Si and purple red highlighting the S. Everything that is not coloured in these maps is therefore graphite or oxides.

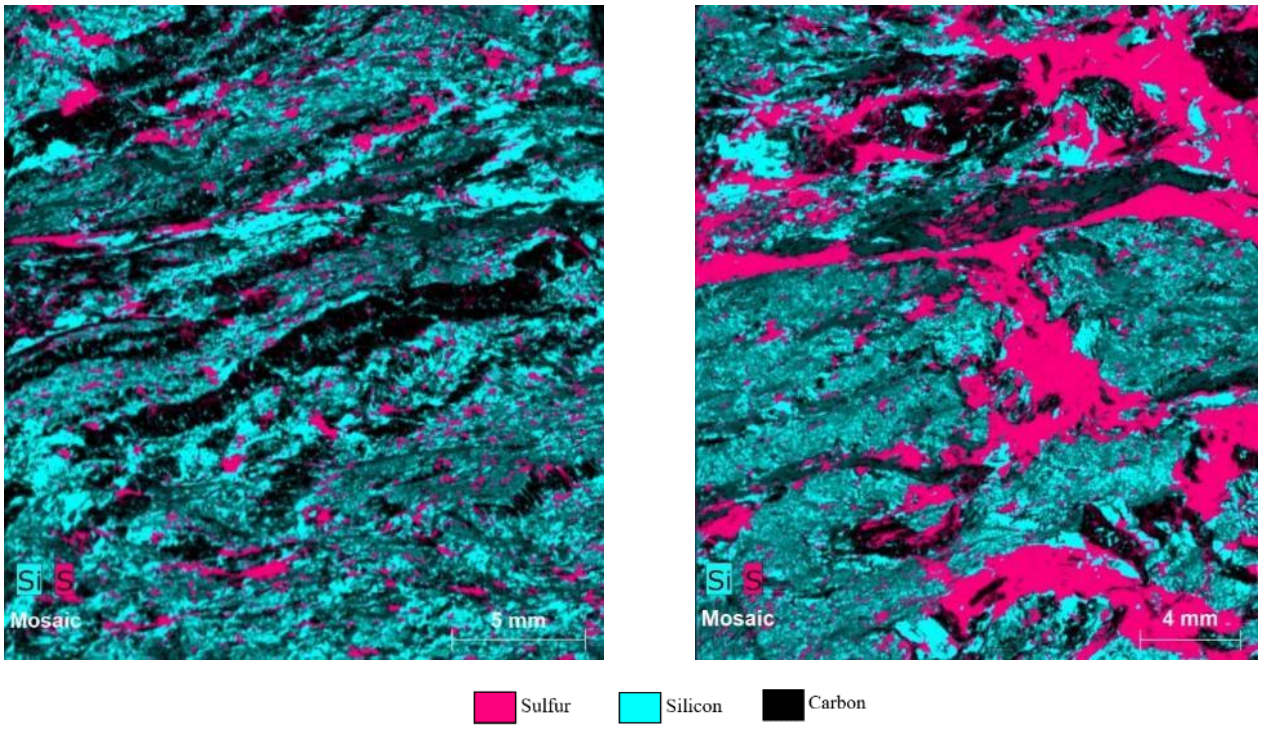

Figure 21: μ-XRF chemical maps of two samples from the ore.

4.4 X-Ray Diffraction

Qualitative XRD analysis (Figure 22) yielded the expected results showing the presence of graphite, quartz, pyrrhotite, biotite and albite, although for the latter mineral not all the peaks were perfectly matching, probably due to a not end member composition. Quantitative analysis was performed but inconsistent with the expected results due to the absence of a correct .cif file (the file that contains the crystalline structure data) in the database of pyrrhotite type in the sample.

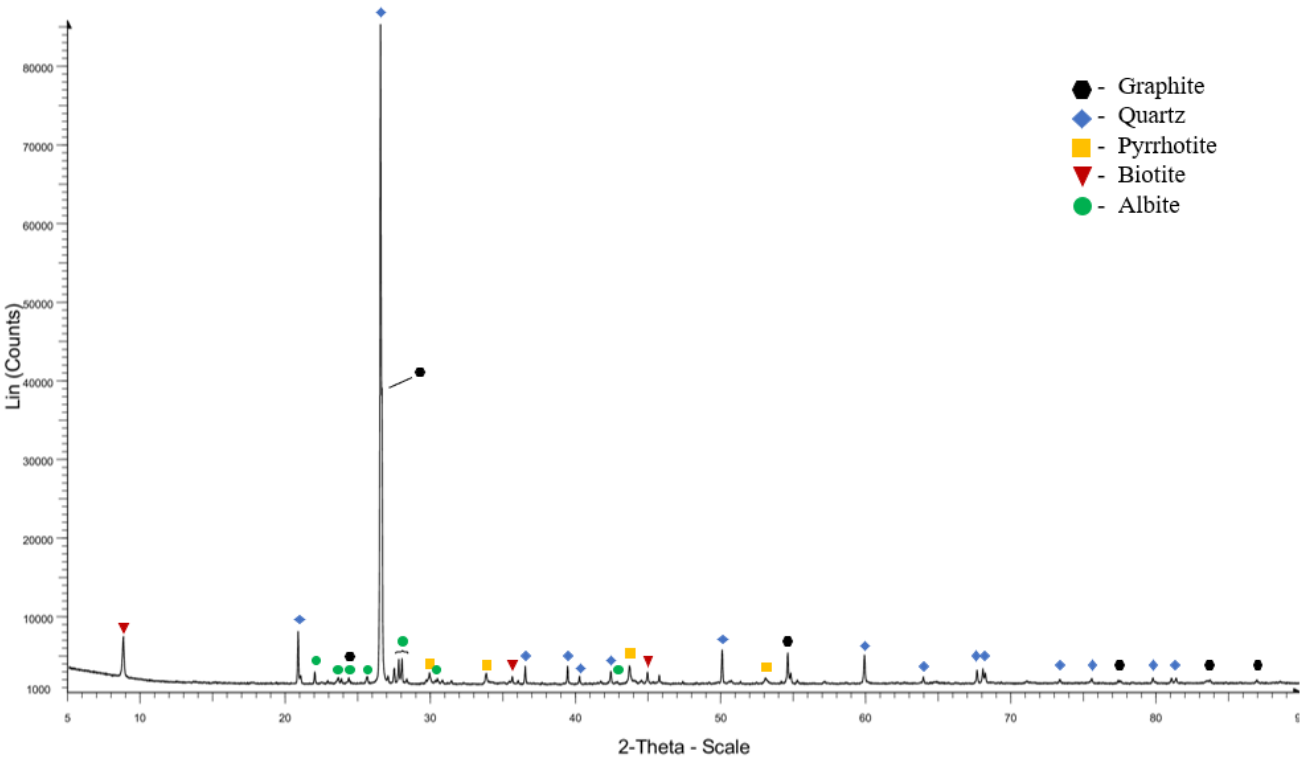

Figure 22: XRD pattern of one sample from the ore body.

4.5 Raman Spectroscopy

Raman analyses were performed on three thin sections, one from the ore body and two from the supposed hostrock. The analyses were performed on graphite flakes and fluid inclusions. The identification of the peaks was done using the rruff database (www.rruff.info) and Frezzotti et al. 2012.

4.5.1 Ore body

On one thin section from the ore, two sites were selected for Raman analysis. One fluid inclusion from a quartz rich area, in which trail of fluid inclusions seems to be departing from graphite flakes and the other site is a basal section of graphite. For graphite analysis, it is important to choose crystals that are not on the surface as the thin section polishing could mechanically modify the structure of the crystals.

The analysis of the fluid inclusions yielded as result the presence of quartz, which is expected given that the fluid inclusion is in a quartz crystal. Hydrocarbons such as methane (CH_4) and ethane (C_2H_6). A small, yet identifiable peak lies in the position comparable to that of molecular hydrogen (H_2) (Figure 23).

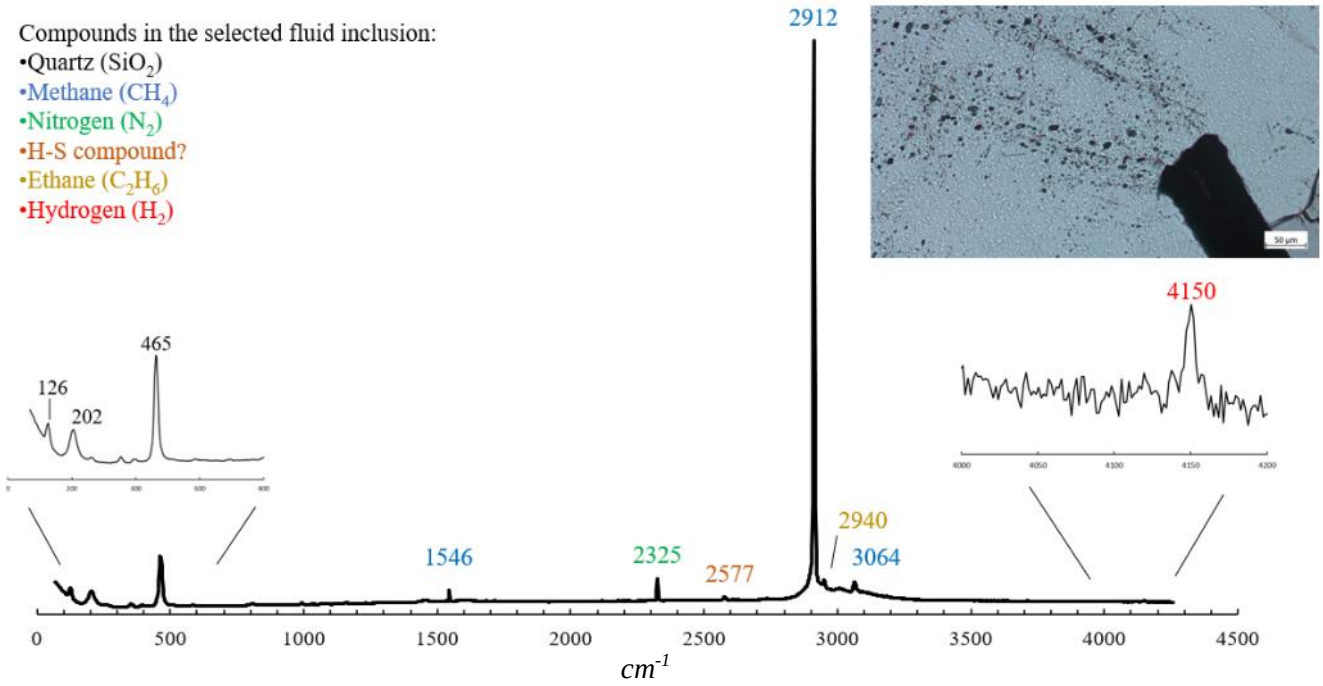

Figure 23: Raman spectrum of fluid inclusion in quartz vein from ore sample.

The second target of Raman analysis is a basal section of graphite (Figure 24) below a feldspar group mineral, most probably albite. All the peaks that are labelled with Raman shift values are peaks that refer to graphite. The height of the peak at 1361cm^{-1}, called disorder peak is a measure of the degree of crystallinity of graphite, the higher the peak the lower the crystallinity of the carbonaceous material (Wopenka and Pasteris, 1993).

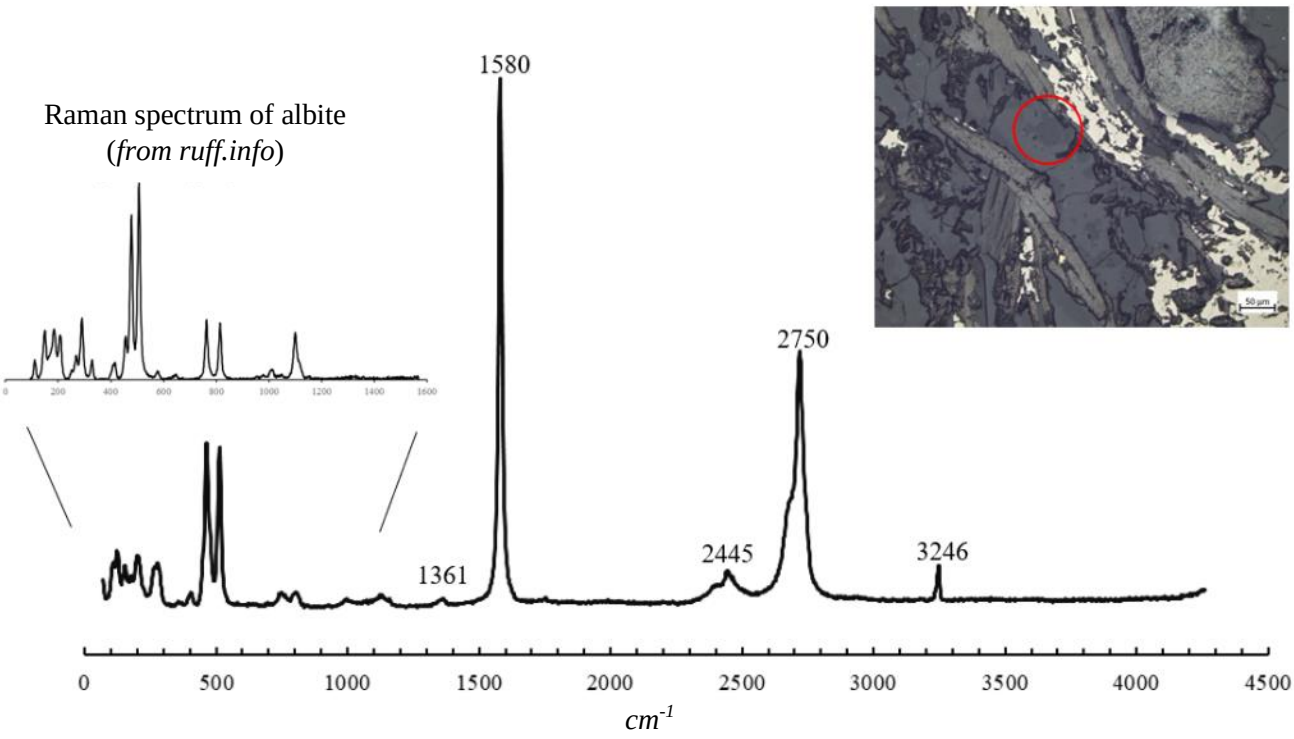

Figure 24: Raman Spectrum of basal graphite in albite crystal from ore sample.

4.5.2 Raman analyses on host rock

The spectrum shown in Figure 25 shows the analysis performed on the liquid part of the fluid inclusion on top of the figure, these liquid results composed of two phases: H_2O and Methane (CH_4). The peaks present in the left area of the graph refer to quartz, hosting the fluid inclusion.

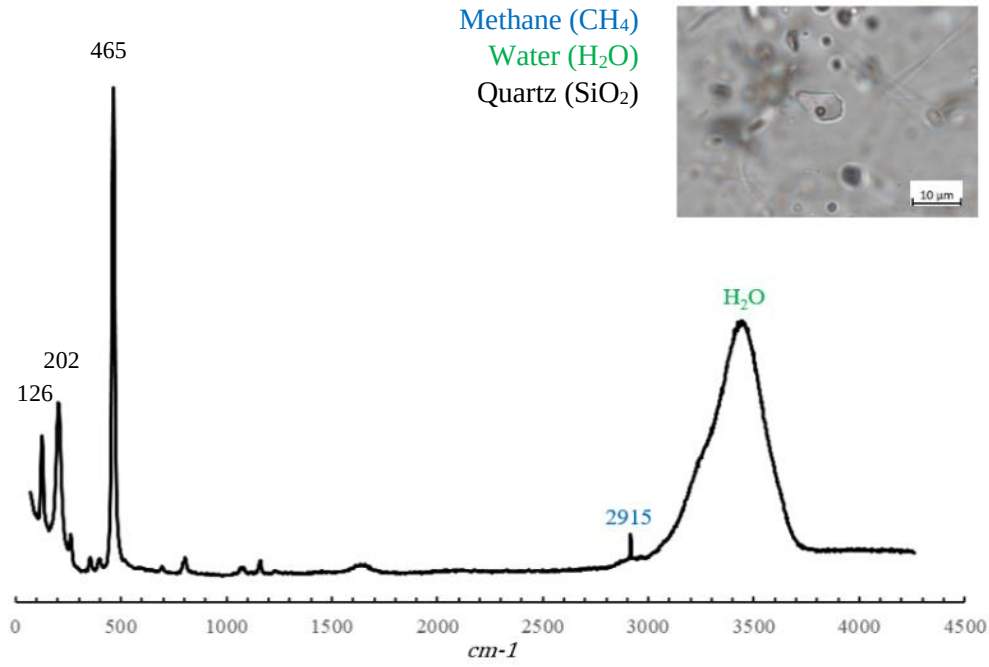

Figure 25: Raman spectrum of fluid inclusion in host rock.

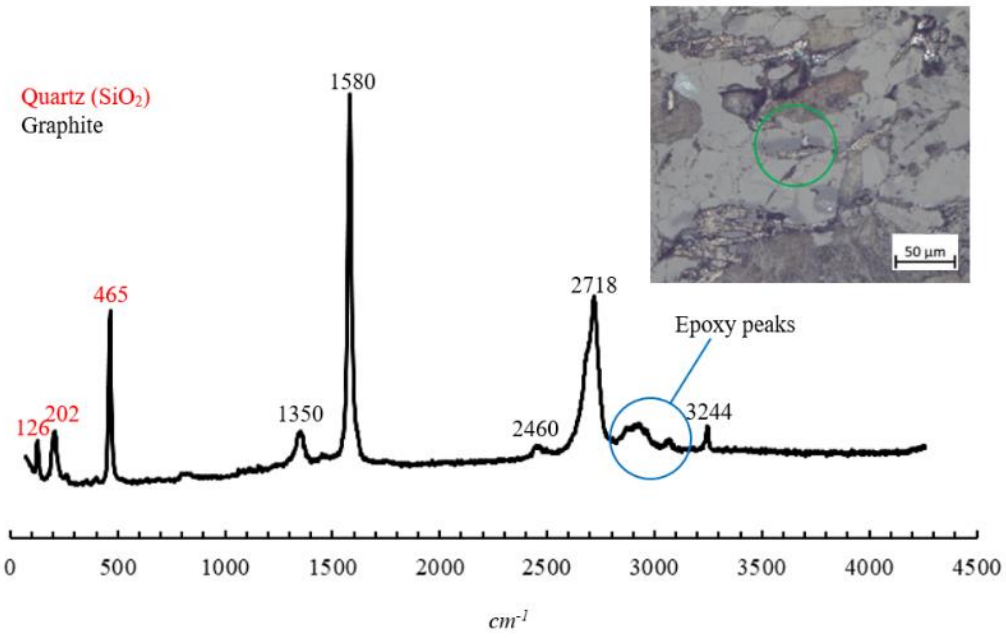

Figure 26: Raman spectrum of graphite flake in a sample from the hostrock.

The spectrum showed in Figure 26 represents the analysis of graphite flake in thin section 546133 from the host rock and it shows that the graphite has a high degree of crystallinity even though the disorder peak in position 1350cm^{-1} is bigger than that in the graphite from the ore.

4.6 Stable Isotope analysis

4.6.1 $\delta^{13}C$

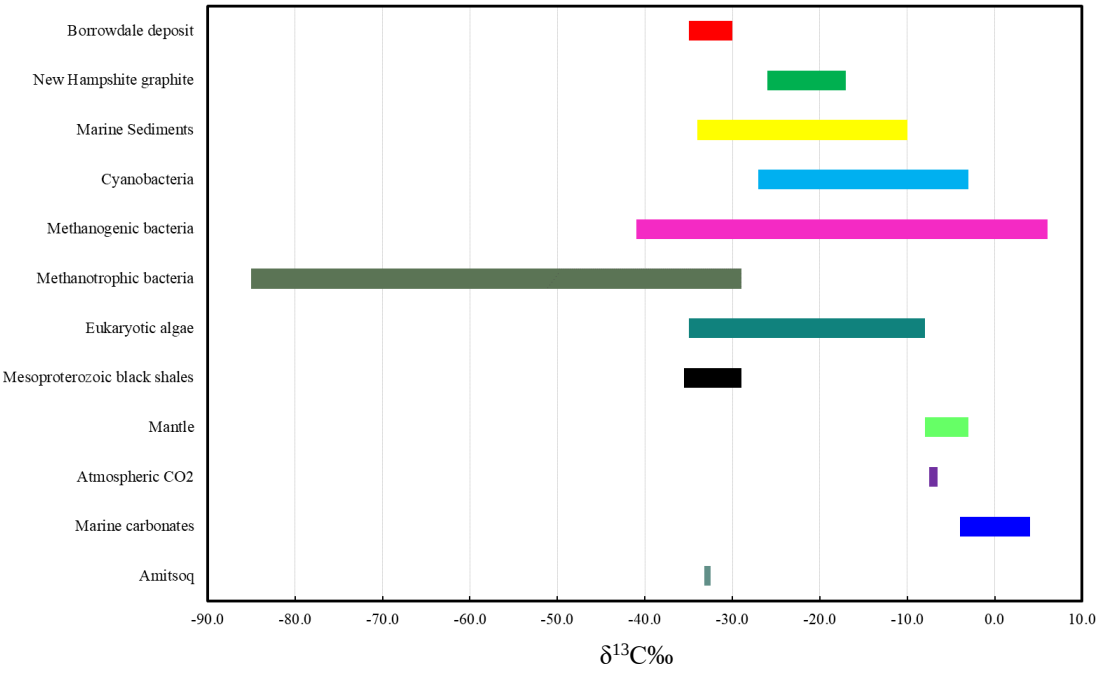

Figure 27: Selected $\delta^{13}C$ values of Amitsoq graphite deposit and possible sources. Organic and marine carbon isotope values are from Schidlowski (1988) and Schidlowski (2001). Mantle values are from Javoy et al. (1986), Deines et al. (1991), and Viljoen (1995). Mesoproterozoic black shales are from Ho et al. (1990), Johnston et al. (2008), and Blumenberg et al. (2012). Carbon isotopes from graphite deposits Luque et al. (2012, and references therein).

$\delta^{13}C$ analysis yielded values ranging from -32‰ to -33‰, a narrow range that overlaps with biotic sources including biogenic (methanogenic and methanotrophic bacteria, Eukaryotic algae) and thermogenic sources, such as Mesoproterozoic black shales.

4.6.2 $\delta^{34}S$

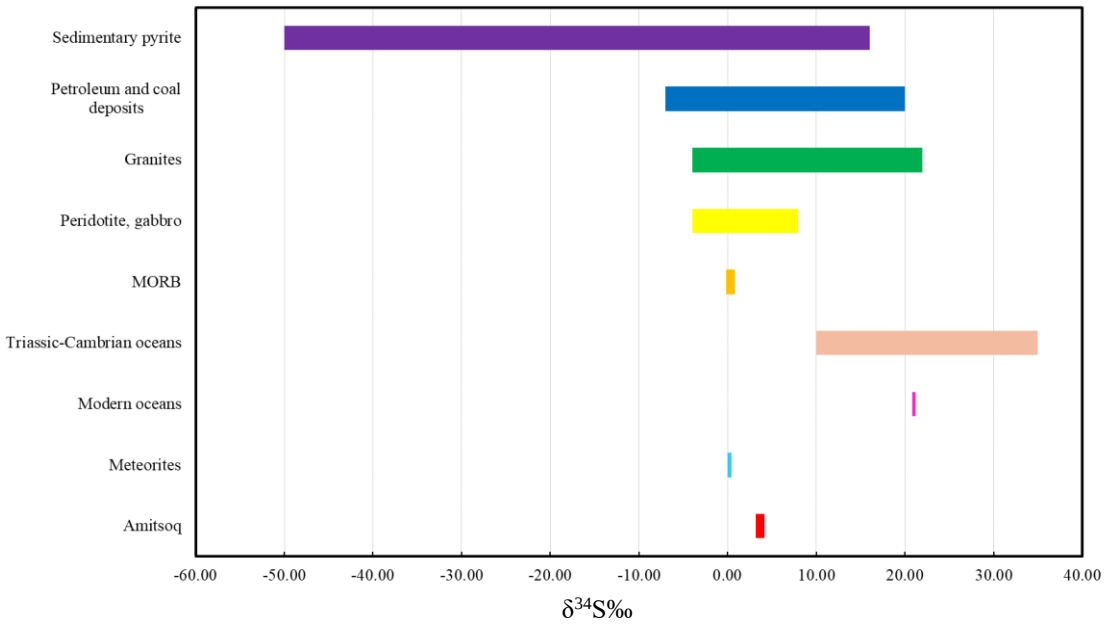

Figure 28: $\delta^{34}S$ values of Amitsoq graphite deposit and selected reservoirs (Nielsen 1979; Seal et al. 2000).

$\delta^{34}S$ analyses yielded values ranging from 3‰ to 4‰, a narrow range that overlaps with several possible sources, both magmatic and of biogenic origin.

4.7 Rare Earths Elements pattern

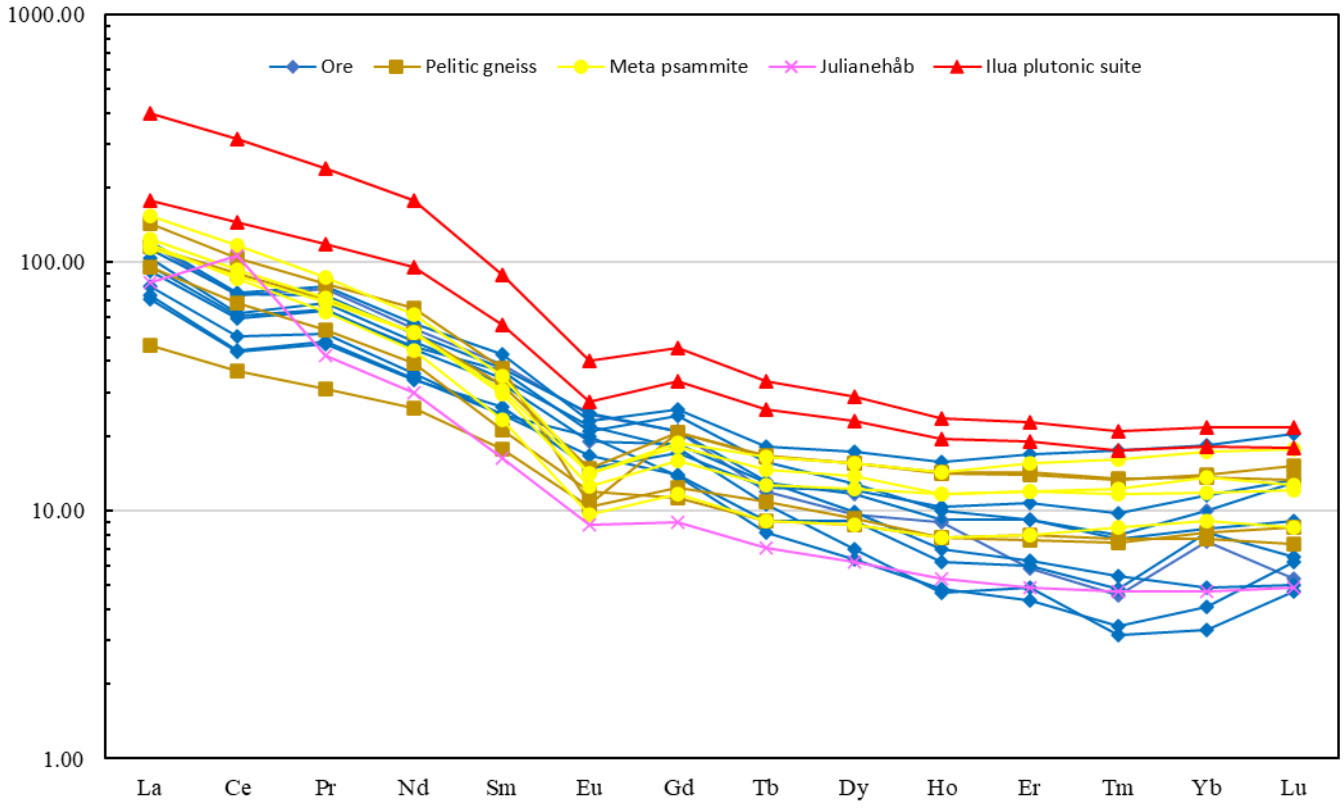

Figure 29 REE pattern of available datasets normalised against "ordinary chondrite" (Nakamura, 1974).

	La	Ce	Pr	Nd	Sm	Eu	Gd	Tb	Dy	Ho	Er	Tm	Yb	Lu
	ppm	ppm	ppm	ppm	ppm	ppm	ppm	ppm	ppm	ppm	ppm	ppm	ppm	ppm
Ore body														
AMI-1	38.90	63.80	10.20	34.10	7.84	1.88	5.73	0.66	3.29	0.69	1.32	0.16	1.66	0.18
AMI-2	31.80	52.40	8.43	28.20	6.56	1.47	5.11	0.71	4.00	0.71	2.06	0.28	2.19	0.44
AMI-3	39.80	65.10	10.45	35.90	8.62	1.76	7.03	0.99	5.95	1.21	3.79	0.61	4.05	0.69
19-1a	24.20	38.40	6.27	21.50	4.92	1.28	3.86	0.50	3.11	0.48	1.34	0.17	1.80	0.22
54-2b	30.50	51.70	8.30	29.00	7.39	1.60	6.68	0.86	4.41	0.77	2.07	0.27	1.86	0.31
73-3a	23.50	37.60	6.13	21.20	5.29	1.14	4.71	0.68	4.12	0.80	2.42	0.34	2.54	0.45
94-4b	34.20	54.20	8.91	30.10	6.92	1.68	4.91	0.58	2.39	0.36	1.10	0.11	0.73	0.16
117-5b	37.00	64.70	9.61	32.60	7.60	1.90	5.77	0.72	3.38	0.54	1.41	0.19	1.07	0.17
139-6b	26.40	43.40	6.72	22.40	4.94	1.54	3.82	0.45	2.19	0.37	0.98	0.12	0.90	0.21
Pelitic gneiss														
535068	47.40	90.00	10.70	41.40	7.60	0.82	5.70	0.92	5.30	1.08	3.14	0.47	3.06	0.52
546101	37.90	78.20	9.19	32.90	6.50	1.14	5.70	0.90	5.30	1.10	3.20	0.47	3.00	0.45
546106	15.20	31.60	4.04	16.20	3.60	0.80	3.40	0.60	3.20	0.60	1.80	0.27	1.70	0.25
546148	31.40	59.40	6.95	24.60	4.30	0.92	3.10	0.50	3.00	0.60	1.70	0.26	1.80	0.29
Meta psammite														
546119	39.00	74.20	8.20	27.90	4.70	0.74	3.20	0.50	3.00	0.60	1.80	0.30	2.00	0.29
546131	37.50	76.00	9.01	32.80	6.20	1.09	5.00	0.80	4.70	0.90	2.70	0.41	2.60	0.41
546158	40.80	80.60	9.38	32.80	6.00	0.96	4.40	0.70	4.20	0.90	2.70	0.43	3.00	0.43
546161	50.50	101.00	11.30	38.70	7.10	1.09	5.20	0.90	5.30	1.10	3.50	0.56	3.80	0.60
Julianehåb														
535066	27.40	92.40	5.50	18.70	3.32	0.67	2.47	0.39	2.14	0.41	1.10	0.17	1.04	0.17
Ilua plutonic suite														
535071	58.40	125.00	15.40	60.60	11.40	2.12	9.13	1.41	7.88	1.49	4.26	0.61	3.96	0.61
535065	131.00	271.00	31.00	112.00	18.00	3.10	12.50	1.82	9.88	1.81	5.12	0.73	4.77	0.74

Table 2: Raw REE data.

The REE patterns of the geological units in the region of interest are plotted in Figure 29, and the raw data are shown in Table 2. Samples from the Ilua Plutonic Suite exhibit a higher REE content compared to the other lithologies and display a negative europium anomaly. The pelitic gneiss and meta psammite samples, as expected, show a similar pattern with a negative europium anomaly. In contrast, the ore body samples exhibit a negative cerium anomaly, a slightly positive europium anomaly, and the HREE pattern varies among the different samples, with some showing positive erbium and/or ytterbium anomalies. Lastly, the only Julianehåb pattern present shows a positive cerium anomaly and a slightly negative europium anomaly.

4.8 Thermobarometry

Thermobarometry involves determining the pressure-temperature (P-T) conditions under which mineral assemblages form, using the principles of equilibrium thermodynamics. The mineral assemblage used in thermobarometry represents a preserved state of equilibrium from a specific part of the P-T path that the rock followed during its formation (Powell & Holland, 2008).

The compositions of coexisting minerals in equilibrium are governed by the thermodynamic properties of the minerals, allowing us to relate them to the pressure and temperature conditions at which they equilibrated.

Thermometers are used to estimate temperature and are based on exchange reactions that are sensitive to temperature but not to pressure. Exchange reactions involve the exchange of cations with similar sizes and charges between two minerals and chemical components being exchanged between phases, so compositions change, but modes remain the same (no phases disappear, and no new phases are produced) (Hirsch, 2023). These reactions are typically very temperature-sensitive but are not pressure-sensitive because no major change in volume

is involved in the exchange. Temperature-sensitive reactions have steep slopes on P-T diagrams (Whitney, 2023).

Barometers, on the other hand, are used to estimate pressure and are based on assemblages that are sensitive to pressure but not to temperature. Barometers are based on pressure-sensitive reactions that involve a significant volume change, they are net transfer reactions, namely reactions in which chemical components being "transferred" from one phase or set of phases to others (new phases are produced as old ones disappear) (Whitney, 2023; Hirsch, 2023)

In order to estimate the P-T formation conditions of the rock units based on the mineral assemblages present in the rock samples, several geo-thermobarometers were considered. This was achieved first by examining the composition of relevant minerals using electron microprobe analysis (EMPA) and then using the following calibrations for minerals pairs that are in textural equilibrium.

- Hornblende-plagioclase geothermometer (Blundy & Holland, 1990; Holland & Blundy, 1994);
- Garnet-clinopyroxene geothermometer (Ganguly, 1979);
- Garnet-biotite geothermometer (Ferry & Spear, 1978; Ganguly et al., 1996);
- Graphite geothermometer (Beyssac et al., 2002).

The Holland and Blundy thermometer could not be used in this case, as the amphiboles present were all low-Ca species, specifically cummingtonite and (ferro)gedrite, rendering the use of this geothermometer impossible. A similar limitation arose when considering the garnet-clinopyroxene geothermometer from Ganguly (1979), as the sample only contained andradite as the garnet species, thus making it unsuitable for this particular geothermometer unless further changes on thermodynamic properties are incorporated.

Garnet-biotite geothermometer

Garnet-biotite geothermometer is based on the cation exchange reaction:

almandine + annite = pyrope + phlogopite

$$Fe_3Al_2Si_3O_{12} + KMg_3AlSi_3O_{10}(OH)_2 = Mg_3Al_2Si_3O_{12} + KFe_3AlSi_3O_{10}(OH)_2$$

and uses the partitioning of Fe and Mg between garnet and biotite that crystallized at equilibrium (Ferry & Spear, 1978). However, establishing whether a specific biotite or a portion of a biotite grain has achieved equilibrium compositions with a particular garnet can be uncertain (Henry & Guidotti, 2002). While criteria for textural equilibrium are important, they do not necessarily imply that chemical equilibrium has been attained or maintained (Guidotti et al., 1991).

In the present study, the solution model used for garnet is based on Ganguly et al. (1996), while for biotite, the Fe-Mg mixing is treated as ideal. As for the mixing of octahedral aluminium and titanium, the model from Patino-Douce et al. (1993) was used.

For the thermometer analysis, two garnet and biotite pairs from sample 546102 were utilized. The corresponding data can be found in Table 3.

	Garnet					Biotite								
	Fe	Fe3+	Mg	Ca	Mn	Si	Ti	Al	Fe	Fe3	Mg	Mn	Cr	Ni
1	2.35	0.00	0.32	0.11	0.18	2.71	0.14	1.60	1.23	0.00	1.19	0.00	0.00	0.00
2	2.33	0.00	0.37	0.11	0.16	2.70	0.12	1.63	1.14	0.00	1.31	0.00	0.00	0.00

Table 3: input values for thermometry.

	Pair 1		Pair 2	
	1	2	3	4
SiO2	37.33	35.85	38.03	36.23
TiO2	0.00	2.52	0.01	2.19
Al2O3	21.99	17.93	22.04	18.53
Cr2O3	0.01	0.00	0.02	0.01
MgO	2.70	10.51	3.22	11.76
FeO	36.17	19.46	36.47	18.24
CaO	1.24	0.05	1.29	0.11
MnO	2.73	0.00	2.35	0.03
Na2O	0.05	0.32	0.00	0.25
K2O	0.02	9.43	0.00	9.28
Total	102.25	96.07	103.43	96.63

Table 4: Major element oxide composition of garnet and biotite pairs as obtained by EPMA analysis for thermobarometry.

	Stoichiometry			
	Pair 1		Pair 2	
	1	2	3	4
Si	2.95	2.71	2.96	2.70
Ti	0.00	0.14	0.00	0.12
Al	2.05	1.60	2.02	1.63
Cr	0.00	0.00	0.00	0.00
Fe3	0.05	0.00	0.05	0.00
Fe2	2.35	1.23	2.33	1.14
Mn	0.18	0.00	0.16	0.00
Mg	0.32	1.18	0.37	1.31
Ca	0.11	0.00	0.11	0.01
Na	0.00	0.05	0.00	0.04
K	0.00	0.91	0.00	0.88
tot. cat.	8.00	7.83	8.00	7.82
tot. oxy.	12.00	11.00	12.00	11.00
Mineral	almandine	biotite	almandine	biotite

Table 5: Stoichiometry calculations of garnet and biotite pairs.

This analysis yielded as result an equilibration temperature of 504°C (± 50°C) for both analysed pairs, estimated at 4kbars.

Graphite geothermometer

Graphite geothermometer estimates the peak metamorphic temperature of carbonaceous material based on Raman spectra (Beyssac et al., 2002).

Raman spectra of metamorphic carbonaceous material exhibit significant evolution with increasing metamorphic grade (Wopenka & Pasteris, 1993) and are sensitive to variations in

metamorphic grade (Beyssac et al., 2002). The graphitization process is generally considered irreversible in most cases, with no effects on the structure of the carbonaceous material during retrogression. Therefore, the degree of organization of the carbonaceous material is considered an indicator of the peak conditions of the metamorphic cycle (Beyssac et al., 2002).

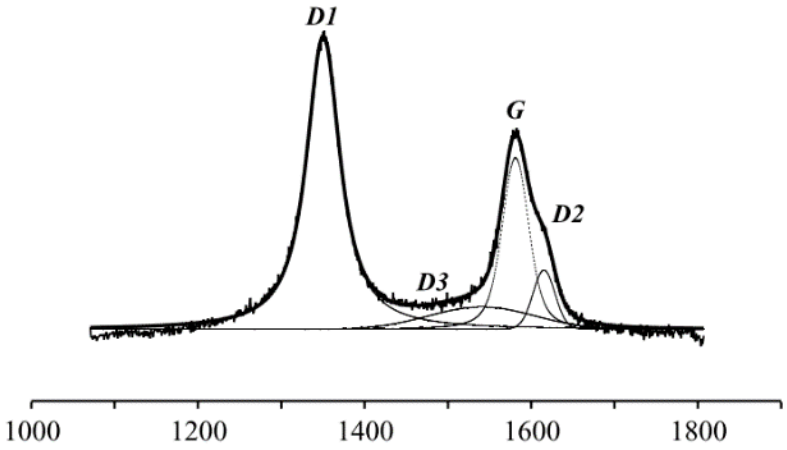

Figure 30: Example of Raman spectrum with labels on different bands (from Beyssac et al., 2002)

Each Raman spectrum of graphite is composed of two regions, further divided in four bands (Figure 30; Tuinstra & Koenig, 1970; Nemanich & Solin, 1979). Using these values, it is possible to define two ratios, peak intensity ratio (R1) and peak area ration (R2) (Beyssac et al., 2002):

$$R1 = \frac{D1}{G}$$

$$R2 = \frac{D1}{G + D1 + D2}$$

The linear correlation between R2 and temperature works in the range 330–650 °C. In the range 330–650 °C for a given value of R2, the maximum error on the estimated temperature is ± 50°C.

This correlation is described by:

$$T(°C) = -445R2 + 641$$

The analysis on a graphite flake from thin section 546133 from the host rock, yielded as result a temperature of 575°C.

4.9 Modelling

In order to model the system that better represents the geological setting of formation of the Amitsoq graphite deposit, several models were produced with ThermotopesCOH and for different conditions. ThermotopesCOH (Boutier et al., under review) is a python-based software, that uses thermodynamic calculations to define the properties and evolution of C-O-H systems in relations with several parameters such as fO_2, $\delta^{13}C$, content of CH_4, CO_2, H_2, H_2O and predicts precipitation of graphite based on these calculations and different

precipitation mechanisms such as desiccation, fluid mixing, temperature changes, and pressure changes.

4.9.1 System definition

Two systems were tested in order to have two scenarios for graphite precipitation: a more oxidised one (System 1) and a more reduced one (System 2). Critical input parameters were selected based on the results of this study and from literature data. In particular:

- Pressure conditions: from the literature is known that in the pelite and psammite zone that host the ore body the pressure values were estimated between 3 and 5kbars (Garde et al., 1998);
- Peak metamorphic temperature of graphite was estimated at 575°C from Raman analysis on graphite flake from the host rock using thermometer from Beyssac et al., 2002;
- $\delta^{13}C$ of graphite is set to -32‰ (Figure 27);

System 1

COH fluid parameters of System 1			
Temperature (°C)	575	Pressure (kbars)	4
Xo	0.786	$CO_2/(CO_2+CH_4)$	0.999
XH_2O	0.238	CO_2/CH_4	1675.834
XCO_2	0.760	fO_2	3.98E-21
XCH_4	0.000	$\log fO_2$	-20.400
XH_2	0.000	Δ Buffer (FMQ)	0
XCO	0.001	fH_2	0.003
aC	1	Graphite	stable
$\delta^{13}C$ Solid	-32‰	$\delta^{13}C$ Fluid	-22.9‰
$\delta^{13}C$ CO_2	-22.9‰	$\delta^{13}C$ CH_4	-35.3‰

Table 6: C-O-H fluid parameters of System 1

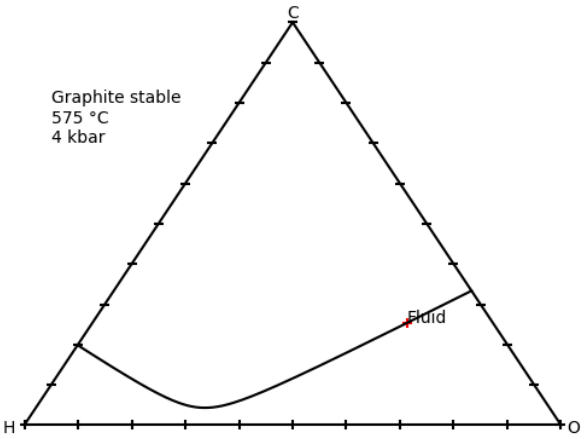

Figure 31: C-O-H diagram with position of fluid from System 1

System 1 is a system defined at fixed ΔFMQ (Fayalite-Magnetite-Quartz) buffer = 0.575 °C and 4 kbars (Figure 31). At these conditions, the only relevant species present in the fluid are H_2O and CO_2 (Table 6; Figure 32) with the latter being dominant. For higher temperatures, the fluid would be entirely composed of CO_2 while at lower temperature CH_4 would become the relevant carbonic species (Figure 32).

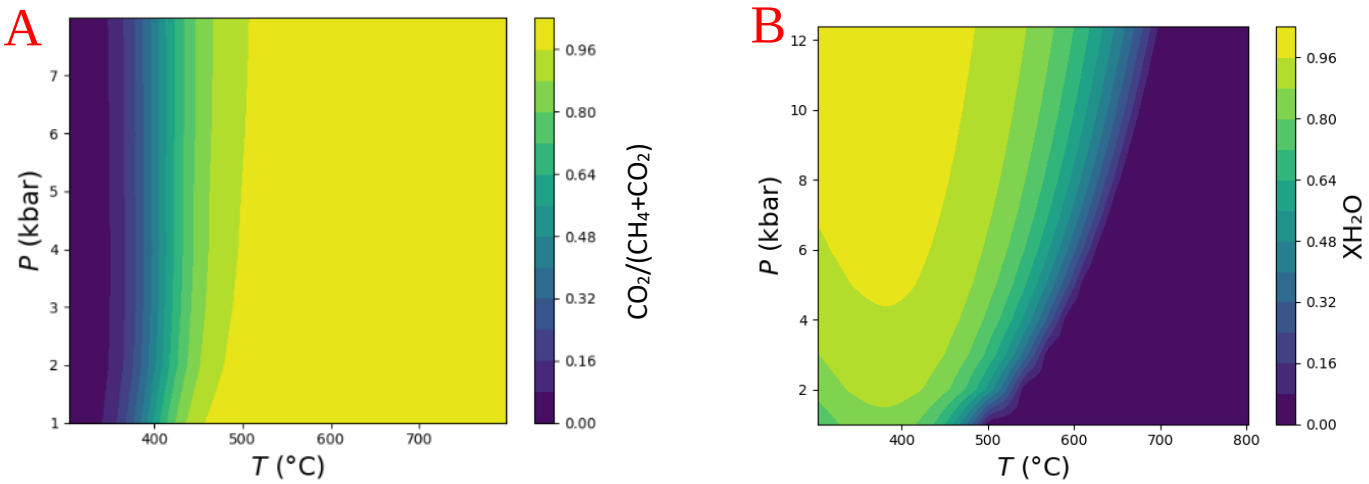

Figure 32: A: Carbonic species of System 1 at different P-T conditions (CO is negligible); B: Water content of System 1 at different P-T conditions.

System 2

COH fluid parameters of System 2			
Temperature (°C)	575	Pressure (kbars)	4
Xo	0.333	$CO_2/(CO_2+CH_4)$	0.506
XH_2O	0.861	CO_2/CH_4	1.026
XCO_2	0.068	fO_2	3.57E-22
XCH_4	0.066	$\log fO_2$	-21.447
XH_2	0.004	Δ Buffer (FMQ)	-1.048
XCO	0.000	fH_2	0.040
aC	1	Graphite	stable
$\delta^{13}C$ Solid	-32‰	$\delta^{13}C$ Fluid	-29‰
$\delta^{13}C$ CO_2	-22.9‰	$\delta^{13}C$ CH_4	-35.3‰

Table 7: C-O-H fluid parameters of System 2

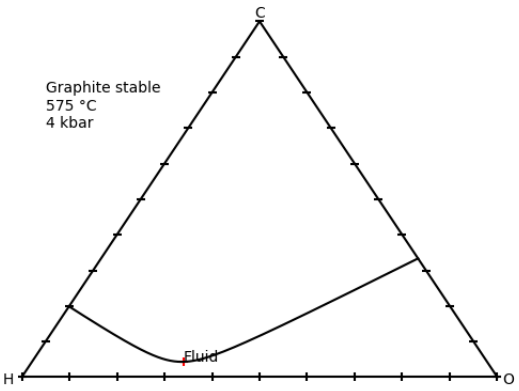

Figure 33: C-O-H diagram with position of fluid from system 2

System 2 is a system based on the hypothesis that the dehydration of a metapelite generates a fluid with a H:O ratio of 2:1, corresponding at $X_O = \frac{1}{3}$ (Connolly&Cesare, 1993) that is therefore fixed in this system (Figure 33). With this assumption, at 575°C and 4 kbars the conditions are more reduced with respect to System 1 and the carbonic species content is different. At the set conditions CO_2 and CH_4 are in equal proportions and the dominant species in the fluid is H_2O, at higher temperatures, both CH_4 and CO_2 increase, maintaining their proportions, while water content decreases (Figure 34).

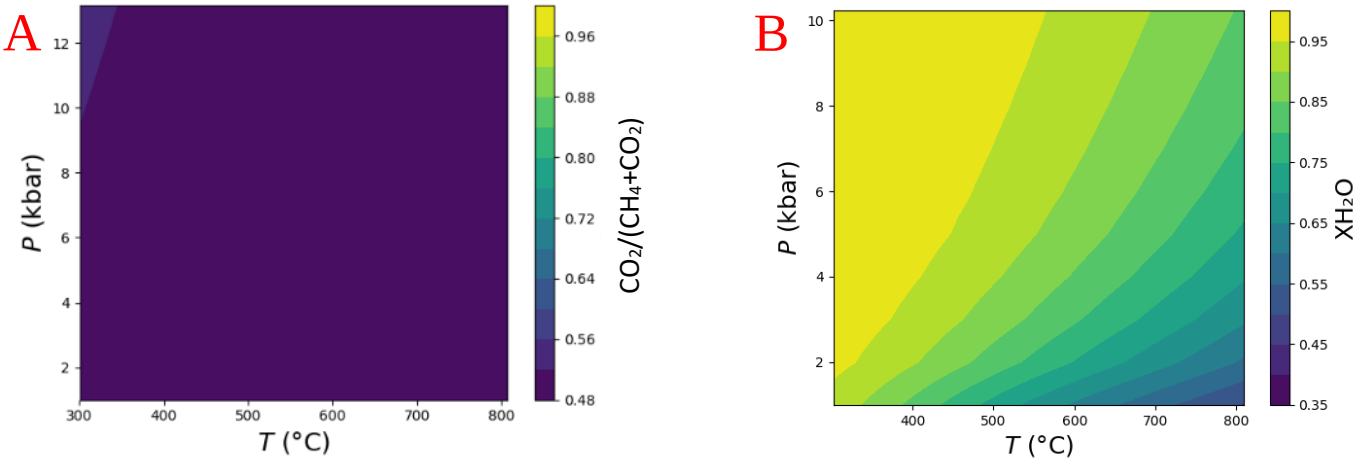

Figure 34: Carbonic species of System 2 at different P-T conditions (CO is negligible); B: Water content of System 2 at different P-T conditions.

4.9.2 Graphite precipitation

Using System 1 and System 2, precipitation of graphite has been modelled using three alternative mechanisms:

- Change in temperature: a change in temperature of a fluid carrying graphite may trigger its precipitation (Frost, 1979);

- Dehydration: desiccation is a process during which a fluid loses water, which results in the progressive increase in the carbon concentration in fluid;
- Fluid mixing: two fluids with distinct characteristics, such as *f*O2 conditions, mix, the abrupt change triggers the fluid deposition (Rumble & Hoering, 1986);

T-Change

This is a cooling process that happens at constant pressure conditions, assuming the change in temperature as the driving process for the graphite precipitation, the most likely geological setting in which this would happen is the emplacement of an igneous body and the subsequent cooling. The area is known for the abundance of granite intrusions, as discussed in chapter 2. A decrease in temperature in this geological setting could be modelled by cooling a magmatic body from 700°C to 550°C (Figure 35; Figure 36).

In the conditions assumed in System 1, a mere decrease in temperature is insufficient to trigger graphite precipitation, as it would only result in the production of CO_2.

At the conditions assumed in System 2, the decrease of temperature triggers the precipitation of 3.3 mol of graphite from 100 mol of fluid with activity of graphite = 1.

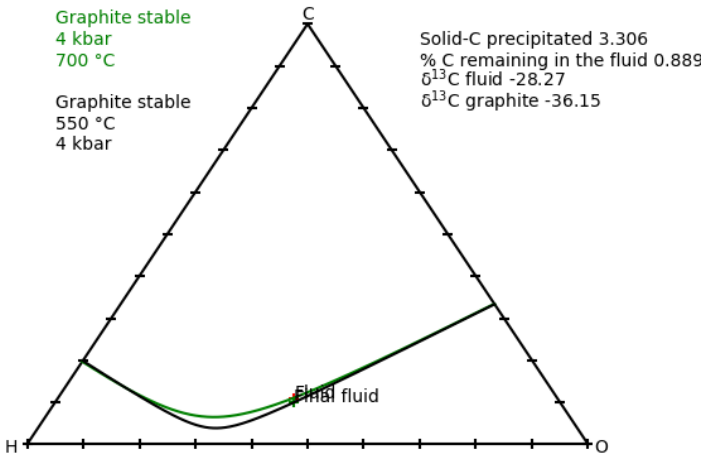

Figure 35: COH system during temperature change, at 700°C (green), 550°C (black).

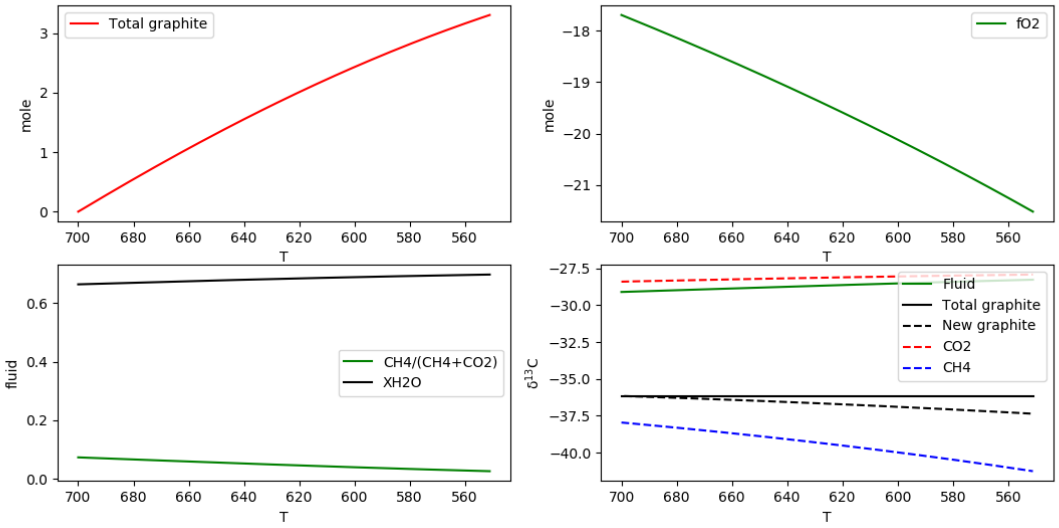

Figure 36: Reaction progress during temperature decrease.

Fluid mixing

Fluid mixing from different source rocks can change the $\delta^{13}C/\ \delta^{12}C$ of the final fluid or $CH_4/(CH_4+CO_2)$ (Figure 38), either of these changes could result in fluctuations in $\delta^{13}C$ of precipitated graphite (Rumble & Hoering, 1986), despite this, all the graphite samples analysed showed a constant and narrow range of $\delta^{13}C$. Mobilization and transport of carbon is accomplished through known metamorphic processes such as devolatilization reactions and propagating hydraulic fractures (Walther & Orville, 1982).

In this model, it is assumed that HT-LP metamorphism dehydrates a pelite, resulting in a fluid with the characteristics of System 2. This fluid then mixes with a fluid at QFM (System 1) (Figure 37).

A similar situation, in which graphite precipitate when CO_2-rich fluid infiltrates low fO_2, rocks under high temperature conditions is described by Lamb & Valley (1984). The process of fluid mixing results to be more efficient in precipitating graphite at these conditions. It is possible to observe that this reaction precipitates more than 11 mol of graphite from 200 mol of total fluid, equally divided between QFM fluid (System 1; 100 mol) and $X_O = \frac{1}{3}$ fluid (System 2; 100 mol)

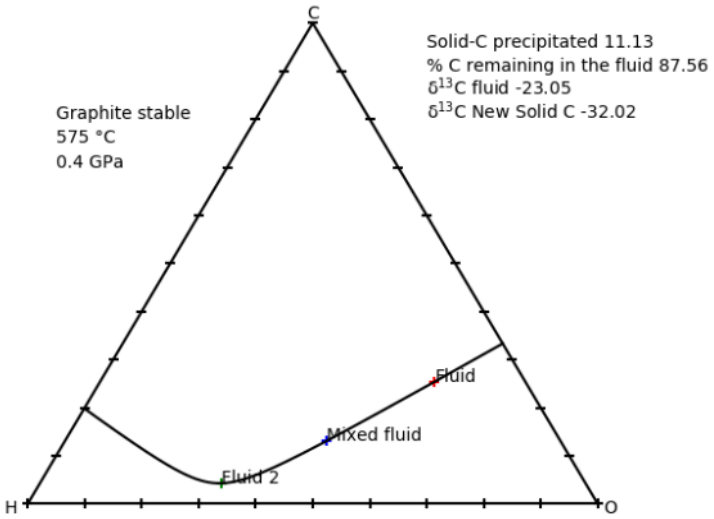

Figure 37: COH system of fluid mixing reaction. "Fluid" represents condition of System 1; Fluid 2 represents condition of infiltrating fluid with characteristics of System 2.

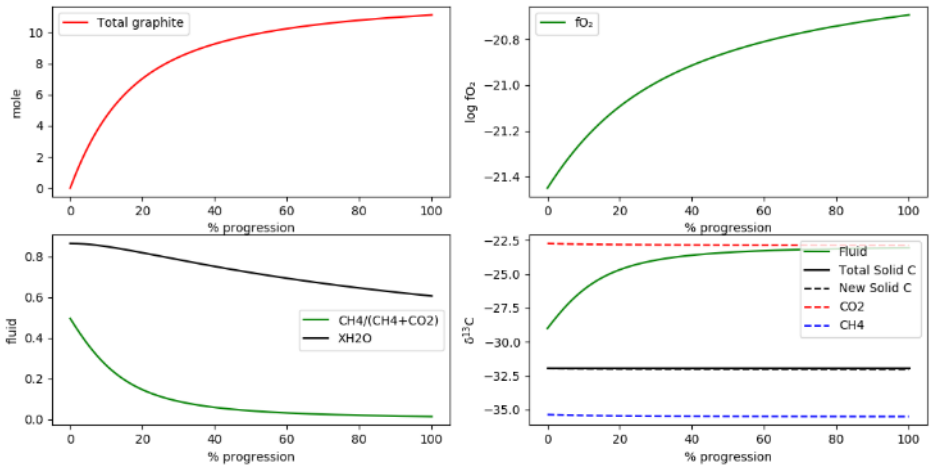

Figure 38: progression of fluid mixing reaction.

Dehydration

System 1

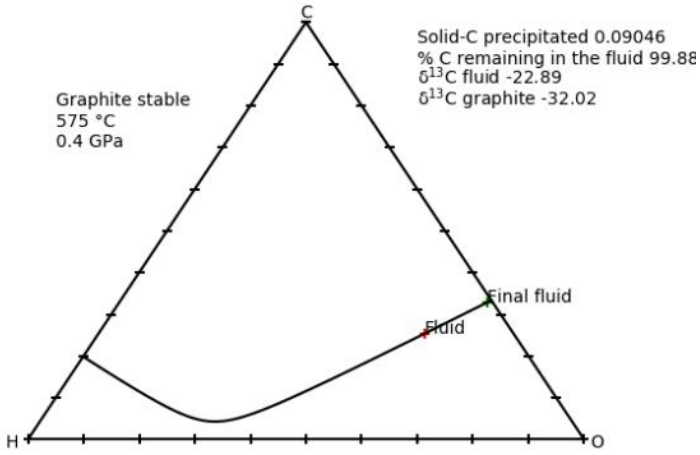

Figure 39: COH diagram of System 1 during dehydration reaction.

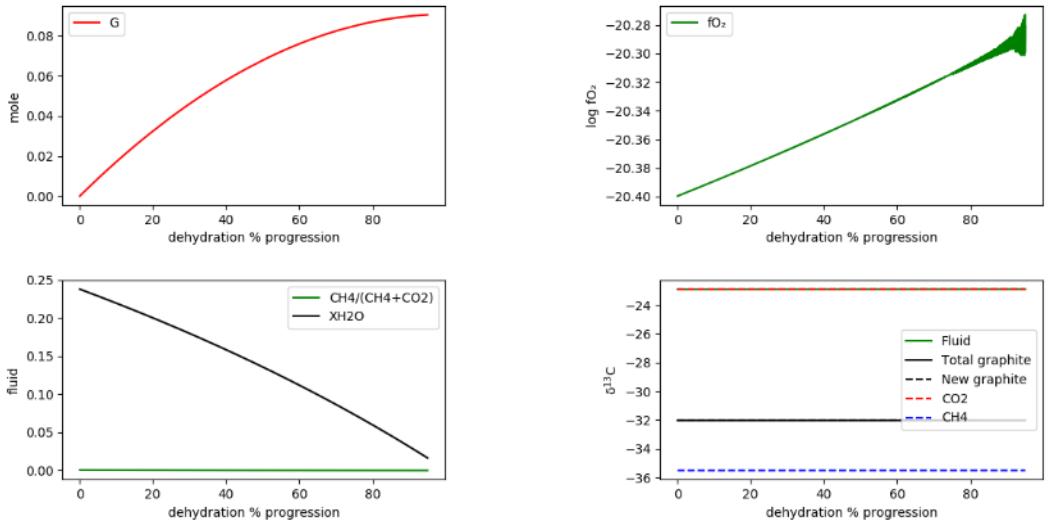

Figure 40: dehydration progression of System 1

Dehydration of a fluid with the characteristics of System 1 at 95% would not be very effective and would result in the precipitation of a minimal amount of graphite, namely 0.09 mol of graphite from 100 mol of fluid. This is because the fluid is predominantly composed of CO_2. The dehydration reaction removes water and precipitates graphite, but since the water content is depleted quickly, the amount of graphite precipitated would be low.

System 2

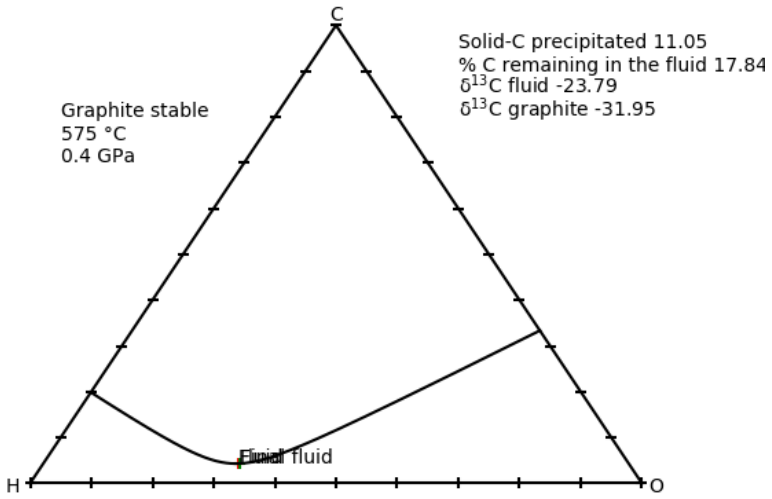

Figure 41: COH diagram of System 2 during dehydration reaction.

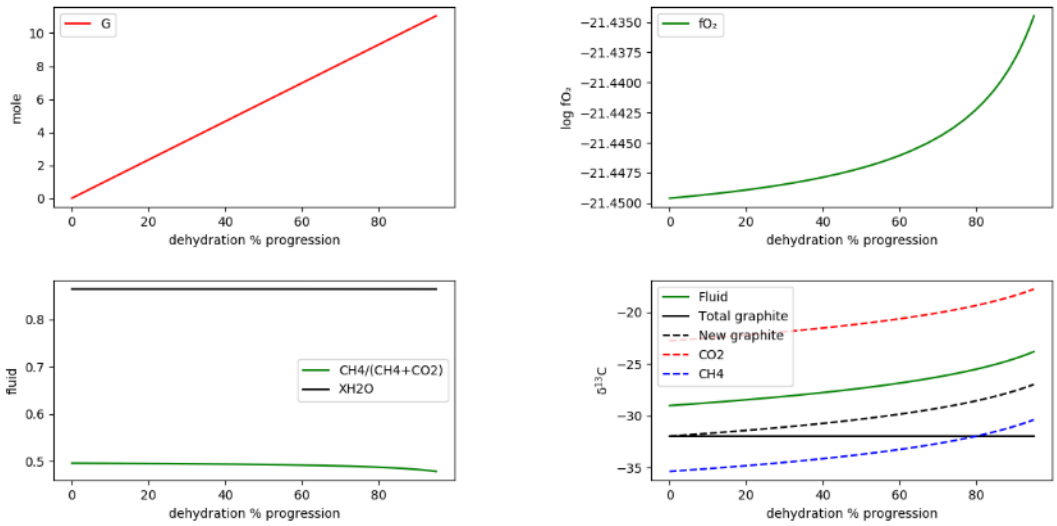

Figure 42: dehydration progression of System 2.

Dehydration of a fluid with the characteristics of System 2 at 95% would be more effective and would result in the precipitation of approximately 11 mol of graphite from 100 mol of fluid with activity of graphite = 1. In this case, the fluid contains a higher amount of water, which is also preserved during the reaction. As the precipitation from methane occurs, hydrogen is released, which subsequently bonds with oxygen to form water (Figure 42).

5. Discussion

5.1 Graphite precipitation

Considering the assumptions made about the conditions prevailing during the formation of the deposit, it is highly probable that the deposition of graphite involved a moderately reduced fluid derived from the host rock, a metapelite. Under high-temperature metamorphism, metapelites tend to produce a fluid composition that closely resembles "water maximum" ($X_O = \frac{1}{3}$) composition (Connolly & Cesare, 1993). This reduced fluid has the tendency to effectively precipitate graphite, both through simple dehydration and through mixing with another fluid at different fO_2 conditions.

Given the geological framework in which the deposit likely formed, it is possible to infer that either one or both aforementioned processes are responsible for graphite deposition. In fact, a combination of dehydration resulting from HT-LP metamorphism and the mixing with a fluid originating from the intense magmatism that characterized the emplacement of the Julianehåb batholith and the Ketilidian Orogeny throughout its history is a plausible scenario.

5.2 Carbon origin

Much of the Earth's estimated 10^{23} g of carbon is sequestered in sedimentary rocks of which 75% is inorganic and 25% is of organic origin (Schlesinger, 1997) and the Amitsoq graphite deposit is an example of how the earth stores carbon over geologically significant time. From $\delta^{13}C$ analysis (Figure 27) it is possible to infer that the origin of the carbon that formed the graphite is compatible with biological processes or the transformation of biogenic material, in particular, three types of organisms have a similar $\delta^{13}C$ as the ore: eukaryotic algae, methanotrophic bacteria and methanogenic bacteria. Given the probable age of formation of the deposit all these three types of early life can be possible source of the organic material that later formed the graphite deposit. Palaeontologists generally agree that an unambiguous record of eukaryotic microfossils extends back to ~1800 Ma (Parfrey et al., 2011), methanogens first appeared long before the deposit, at ~3500 Ma (Wolfe & Fournier, 2018), and methanotrophic signatures are present in the Archaean and Paleoproterozoic record (Schidlowski, 2001).

5.3 Fluid inclusions

5.3.1 Carbonic species

The carbon in the sedimentary rocks that formed the Amitsoq graphite deposit may have been initially subjected to maturation by diagenesis and subsequent HT-LP metamorphism during which the kerogen, which constitutes the organic matter, became more ordered and compacted as fluids were released. There is abundant evidence that carbonic fluids are produced during metamorphism of organic-rich shales (Crawford and Hollister, 1986; Rumble et al., 1986; Mullis, 1987; Duke et al., 1990b; Olsen and Ferry, 1995; Bergfeld et al., 1996; Hurai et al., 1997; Luque et al., 1998; Touret, 2001; Schwab et al., 2005).

Among factors that may influence fluid compositions in the deep crust are the equilibrium relationships between the fluids and the mineral assemblages in the host rocks and the mutual solubilities of aqueous and carbonic components (Huff & Nabelek, 2007).

During degradation of organic matter and dehydration of the sedimentary rock during early metamorphism, carbonic fluid will be dominated by reaction of H_2O with graphite (Ohmoto and Kerrick, 1977; Frost, 1979; Connolly and Cesare, 1993; Connolly, 1995).

Following graphitization of organic matter, and in the absence of a mineral fO_2 buffer or infiltration of external fluids, fluid speciation will be controlled by the reaction (Ohmoto and Kerrick, 1977; Frost, 1979; Holloway, 1984; Connolly and Cesare, 1993):

$$2C + 2H_2O \rightarrow CO_2 + CH_4$$

This reaction will produce equimolar concentration of CO_2 and CH_4, but in the presence of a redox buffering mineral assemblage the fluid composition may consist either of CO_2-H_2O or CH_4-H_2O (excluding minor components such as H_2 and CO or more complex hydrocarbons), depending on the temperature of the ongoing dehydration reactions (Huff & Nabelek, 2007).

5.3.2 Hydrogen

The analysed fluid inclusion from the ore showed evidence of molecular hydrogen (H_2). The analysed fluid inclusions are part of trails of fluid inclusions in a coarse quartz vein and that propagate from graphite flakes, thus the formation of these fluid inclusions may be interpreted as a secondary process with respect to the deposition of graphite. There are several H_2-producing fluid-rock interaction processes, some of which are: serpentinization (Schulte et al., 2006; Sleep et al., 2004), formation of FeS_2 from FeS (Drobner et al., 1990), thermal decomposition of alkanes and carboxylic acids (Seewald, 2001), oxidation of Fe^{2+}-bearing minerals (Stevens and McKinley, 1995), and fracture-induced reduction of water (Kita et al., 1982), and radiolytic decomposition of water (Lin et al., 2005a, 2005b).

Serpentinization

Hydration of ultramafic rocks forms serpentine and hydroxides (Sherwood et al., 2007):

$$Fe_2SiO_4 + 5Mg_2SiO_4 + 9H_2O \rightarrow 3Mg_3Si_2O_5(OH)_4 + Mg(OH)_2 + 2Fe(OH)_2$$

is coupled with oxidation of Fe^{2+} to form magnetite and H_2 gas:

$$3Fe(OH)_2 \rightarrow Fe_3O_4 + 2H_2O + H_2$$

This reaction commonly takes place at the bottom of the ocean or where fluid interacts with mafic or ultramafic rocks. This is not the case in the geological context of the evolution of the Ketilidian orogen, hence it is unlikely that the hydrogen found in the fluid inclusion from the ore in Amitsoq comes from this process.

Pyrite formation

The formation of pyrite (FeS_2), a key factor in determining the global redox balance (Jorgensen, 1989). Two of the geochemical environments in which pyrite forms are:

sedimentary systems, in which pyrrhotite (FeS) is rare and in which pyrite seems to be formed from amorphous FeS (Berner, 1970; Boesen & Postma, 1988), and hydrothermal systems in which pyrite may be formed not only from amorphous FeS but also from pyrrhotite (Hall, 1986). The reaction (Drobner et al., 1990):

$$FeS + H_2S \rightarrow Fe(SH)_2$$

$$Fe(SH)_2 \rightarrow FeS_2 + H_2$$

May be relevant in the context of the Amitsoq graphite deposit to justify the presence of hydrogen in late-stage fluid inclusion. Potential H_2S hydrothermal fluid interacting with the abundant pyrrhotite present in the rock formation may have generated H_2 that then reacted with graphite with the reaction:

$$C_{graphite} + H_2 \leftrightarrow CH_4$$

this would explain both hydrogen and methane in the ore fluid inclusion, but it is still a tentative interpretation and more proof for this type of hydrothermal event would be required to assess a plausible model.

Radiolysis

Radiolytic H_2 is produced through dissociation of water by α, β and γ particles released during radiogenic decay of U, Th and K. These particles dissociate H_2O into e^-, H^+, H and OH radicals, H_2 and H_2O_2, which then react within μs to yield H_2, O_2, and H_2O_2 (Spinks and Woods, 1990). Unlike all the other mechanisms which depend on a combination of geochemical and mineralogical species, the radiolysis of water only requires water and radioactive elements such as potassium, uranium or thorium and will diminish with the slow decay of the radiogenic elements (Lin et al., 2005a). In the context of the Amitsoq deposit the age (1.7Ga) and mineralogy (presence of uranium) matches with the requirements to produce hydrogen via radiolysis (Sherwood et al., 2014).

5.3.3 Nitrogen

The analysed fluid inclusion from the ore showed presence of Nitrogen (N_2) in CH_4 bearing fluid inclusions, this suggests that the trapped fluids were produced during early metamorphism (Huff & Nabelek, 2007). This can happen during destruction of organic matter as the temperature increases (Mullis, 1987) and can continue to high-temperature metamorphic conditions with the release of ammonia from phyllosilicates, clays, or micas (Bebout et al., 1999; Hurai et al., 2000; Sadofsky and Bebout, 2000). Fluid inclusions in the host rock instead do not show any sign of nitrogen.

5.3.4 Competing carbon and hydrogen storage

The results obtained with Raman spectroscopy showed the abundance of methane in fluid inclusions from the ore, specifically in fluid inclusions in a late-stage quartz vein that propagate from graphite flakes. The presence of hydrogen in these fluid inclusions is a feature that may indicate interactions between graphite and hydrogen: the interaction between hydrogen and graphite generates methane.

This kind of reaction has been suggested in H_2-rich metamorphic environments by Vitale Brovarone et al. (2017) and demonstrated experimentally by Pena-Alvarez et al. (2021). The

impact of this interaction is manyfold and may represent an important process to consider in the current effort to mitigate global warming. Graphite precipitation is in fact a natural process of carbon storage. However, despite precipitating graphite may be an effective way to store CO_2 in crustal rocks, and storing H_2 in crustal reservoirs is a fundamental green energy target (Muhammed et al., 2022), the interaction between hydrogen and graphite may pose the problem of methane generation. Methane is in fact a much more potent greenhouse gas relative to carbon dioxide (Howart, 2014). Particular caution should therefore be used when considering storage sites for carbon and/or hydrogen reservoirs.

5.4 Age of the deposit

From the literature, banded quartz-graphite-sulphide rocks are known to overlie meta-sedimentary units and form an important marker horizon at the base of the Nanortalik nappe at Nalunaq Mountain (Olsen and Petersen 1995; Kaltoft et al. 2000). With the assumption that these quartz-graphite-sulphide rocks are the same lithological unit as the ore, it is possible to infer a timespan in which the ore must have formed.

By 1795 Ma, when the Julianehåb batholith had grown sufficiently large and stable to become uplifted and unroofed, immature erosion products from the batholith were deposited (Garde et al., 2002).

A first stage of deformation started right after, a D_1 phase which is dated at >1792Ma (Garde et al., 2002), this sets the upper limit for the ore body formation in Amitsoq. This is contemporaneous with the end of arc-type magmatism in the Central Domain of the Julianehåb batholith and the deposition of first sedimentary rocks, as constrained by zircons to ca. <1793Ma (Bell et al., 2017; Garde et al., 2002). After the D_1 phase a D_2 phase associated with regional HT-LP metamorphism with numerous granitic intrusions between 1795 and 1785Ma (Garde et al., 2002).

These two earliest phases of deformation (D_1-D_2) were essentially coaxial and coplanar and gave rise to flat-lying structures with intense composite S1–S2 LS fabrics and tight to isoclinal folds (Chadwick et al. 1997; Garde et al. 1997) that can be seen in some of the studied thin sections.

The “Main Vein” of the Nalunaq gold deposit, reported by Bell et al. (2017), postdates the quartz-graphite-sulphide rocks in the Nanortalik nappe and its time frame of mineralisation is ca. 1783–1762 Ma, that coincides with regional D3 deformation in the Southern Domain, dated to ca. 1786–1778 Ma.

It is therefore possible to infer an age of mineralisation between 1793-1762Ma, keeping as constraint its formation before the gold mineralisation that therefore can narrow this time frame.

The Paleoproterozoic age of the deposit is not a coincidence, as, of the thirty-three richest graphite deposits in the world (minimum 8 wt% carbon), twenty-eight are of Palaeoproterozoic age (Figure 43) (Parnell et al., 2021).

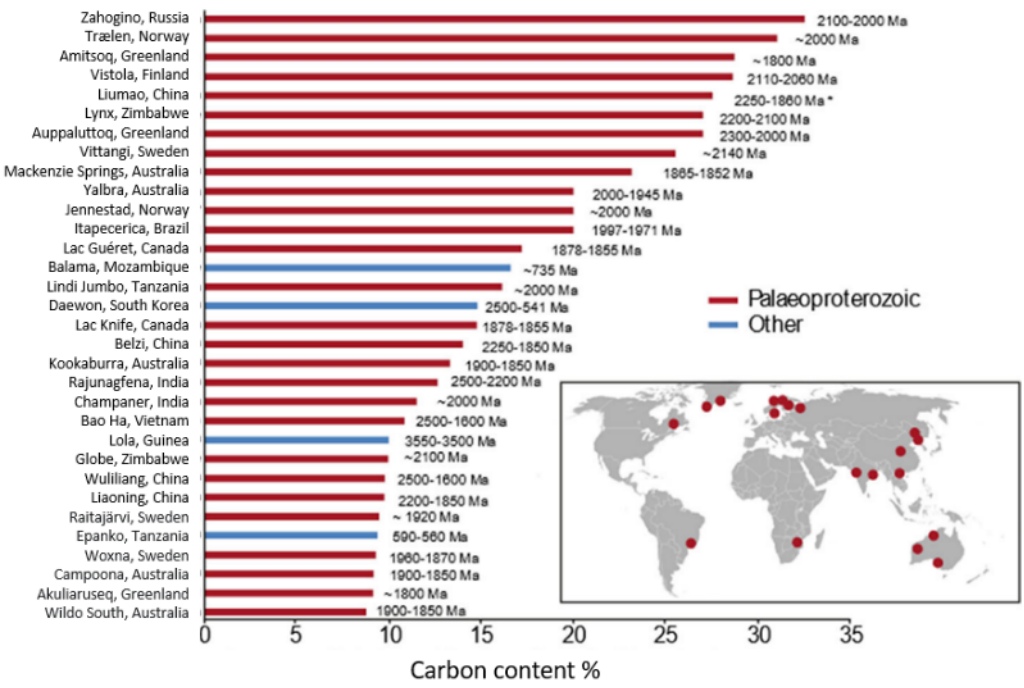

Figure 43: Carbon content and approximate age of the thirty-three richest graphite deposits in the world (from Parnell et al., 2021).

The abundant carbon required for the formation of these deposits may reflect intense weathering of continents following the Great Oxidation Event (~2.4Ga; Gumsley et al., 2017) and high productivity in the nutrient-rich oceans (Melezhik et al., 2013). The deposition of carbon may also be related to the Lomagundi–Jatuli Event that was a major anomaly in the global cycling of carbon which records a positive excursion in $\delta^{13}C$ composition in carbonates worldwide (Melezhik et al., 2007), happened ~2.2Ga. That was followed by the ~2.0Ga Shunga event, characterized by the deposition of extensive black shales on several continents (Condie et al., 2001; Strauss et al., 2013; Martin et al., 2015).

Therefore, the formation of the Amitsoq graphite deposit must be seen as part of a global trend of high carbon deposition rate during the Paleoproterozoic. In fact, the high carbon accumulation during the Palaeoproterozoic coincided with a high crustal preservation potential, related to supercontinent assembly (Condie et al. 2001; Condie, 2014), leading to the long-term survival and mineralizing legacy of the Palaeoproterozoic carbon reservoirs.

5.5 Rare Earths Elements pattern

Normalized REE distribution patterns are a valuable geochemical tool because they display the normalized REE concentration level and anomalies of Ce, Eu and, Yb. Deciphering the "REE code" reveals information on several aspects of fluid composition and physico-chemical environment of mineral formation (Bau & Möller, 1991). The behaviour of a trace element in geochemical systems can be broadly regarded as a consequence of its ionic charge and ionic radius (Bau, 1991).

Anomalies in normalized REE patterns result from valency changes of REE ions compared to their immediate neighbours in the REE series, because the change in oxidation state is accompanied by a change in ionic radius (Bau & Möller, 1991).

A negative Eu anomaly is typical of many continental rocks, as well as most sediments and seawater (White, 2005). The Eu anomaly arises because many crustal rocks of granitic and granodioritic composition were produced by intracrustal partial melting, the residues of those melts were rich in plagioclase, hence retaining more of the Eu in the lower crust, and creating a complimentary Eu depleted upper crust (White, 2005). Sediments and seawater inherit this Eu anomaly from their source rocks in the upper continental crust (White, 2005), this would explain the Eu anomalies present in the granitoids body and metasedimentary rocks (that compose the hostrock).

Relative to feldspar rich rocks, the sericitic alteration showed a dramatic increase in the size of the negative europium anomaly. The major alteration reaction involved breakdown of plagioclase and K-feldspar, both of which have large positive europium anomalies and contain Eu^{2+} (Sverjensky, 1984). This may explain the negative europium anomaly in all the considered lithologies, the absence of a pronounced anomaly in the ore may testify for a fluid that enriched the assemblage in LREE.

The only sample from Julianehåb shows a positive Ce anomaly whereas the samples from the ore all show a slightly negative Ce anomaly. Negative Ce anomalies are well known from sea and river waters (Elderfield, 1990) while according to Bau & Möller (1991) the generation of Ce anomalies in high-T environments seems unlikely. This is in contrast with what is observed and expected. Given that only one sample from the Julianehåb complex has been analysed this can be an error in the measurements or sampling target, while for the anomaly in the ore it may testify for a later stage low-T fluid that generate the negative anomaly.

6. EIT Raw Materials chapter

This master thesis is done as a conclusive work of EIT-labelled master's in Raw Materials exploration and Sustainability (RaMES).

6.1 Graphite as a critical raw material

Graphite is an opaque, grey-black, and soft (1-2 on Mohs hardness scale) mineral with a metallic lustre. It is characterized by a greasy feel, low density (2.09-2.23 g/cm^3), high resistance to thermal shock, and high electrical conductivity (Anthony et al., 1990). Inertness, compressibility, elasticity, and lubricity are other important physical properties (Wissler, 2006). The 2022 world natural graphite production was estimated at 1.3 million tonnes, with a 15% increase with respect to 2021, with most of it originating in China (65%), Mozambique (15%), Madagascar (8%), Brazil (7%), Russia (1%), Canada (1%) and other minor producers to account for the remaining 5% (Garside, 2023). The most important applications for graphite are as a component in advanced and green energy technologies that

rely on Li-ion batteries and refractories for steel production, and is, for these reasons, classified as a critical mineral (Taylor, 2006; European Commission, 2020).

In recent years, the growth in awareness of the need to create a stable supply chain for CRMs, increased the interest in the raw materials value chain. Although secondary sourcing through recycling is particularly important this is not sufficient to supply the needs of the growing market of EVs and batteries in general, products for which graphite is of outmost importance.

6.2 Hydrogen as player in energy transition

Hydrogen is not a raw material sensu strictu but, being a potential future green source of energy, it aligns to the scopes of the EIT Raw Materials. Hydrogen is the most abundant and simple substance of the universe (Dunn, 2002; Momirlan & Veziroglu, 2005). It has energy per mass content of 143 MJ kg^{-1}, a figure which is up to three times larger than liquid hydrocarbon-based fuels (Ahluwalia & Peng, 2009), its consumption comes with minimal harmful emission (Verhelst & Wallner, 2009) and the byproduct is only water (Schlapbach & Borgschulte, 2008).

As discussed in chapter 5, there are several possible natural processes that produce hydrogen. However, up until now fossil-based fuels are still the main recourse for industrial mass scale hydrogen production (Mazloomi & Gomes, 2012). Fossil fuels have large and heavy hydrocarbon based molecular structure and extracting hydrogen by breaking the bonds between hydrogen and carbon content is one of the most popular methods of hydrogen production (Padro & Lau, 2002). Nowadays, steam-methane reforming (SMR) is known as the most economical method (Balat, 2008) and the reaction of this highly endothermic process is given by:

$$H_2O + CH_4 \leftrightarrow CO + 3H_2$$

Hence producing harmful carbon monoxide.

Another production method is producing hydrogen from water by means of electrolysis: water is subjected to an electric current in order to force its molecules to decompose (Schoots et al., 2010):

$$H_2O \leftrightarrow H_2 + \frac{1}{2}O_2$$

this method does not have a large share in global hydrogen production, due to high production costs, low conversion efficiency, and electrical power expenses (Dunn, 2002; McDowall & Eames, 2006; Ivy, 2004; Jørgensen & Ropenus, 2008) moreover electricity is not always produced from renewable sources, making this method not necessarily “green”.

Hydrogen can be an important player in energy transition, but its production has to shift towards electrolysis or direct sourcing from rock reservoirs.

6.3 EIT OLO alignment

6.3.1 EIT OLO 2 - Innovation skills and competencies

This study was conducted to investigate a deposit whose existence has been known for at least one hundred years but whose origin and genesis remained pretty much unknown and

unstudied by the scientific community. These types of studies, of deposit of commodities fundamental for the green transition, can help future exploration and future consideration of some other previously unconsidered exploration targets or increase the knowledge of already known deposit, shading a new light on the behaviour of mineralising fluids. Moreover, potential future consideration on the role of hydrogen in the deposit was never considered and may increase the interest on the deposit. The use of standard and new analytical/modelling techniques increased the innovation skills and competencies of the author.

6.3.1 EIT OLO 4 – Intercultural skills and competences

This study was conducted involving different organizations and research institutions. It involved firstly GreenRoc Mining plc, which is a junior mining company operating in Greenland and owning the licence in the Amitsoq region. Regarding the public sector, this study involved the participation of the Geological Survey of Denmark and Greenland (GEUS), the Early Earth Research Group of the University of Copenhagen led by Professor Kristoffer Szilas and by the Deep Carbon Laboratory of the University of Bologna led by Professor Alberto Vitale Brovarone who is the supervisor of this master thesis. Conducting this study across two different countries (Denmark and Italy) and involving partners from the private and the public sector increased the intercultural skills and competences of the author.

7. Conclusion

Despite being known for more than one hundred years, the Amitsoq graphite deposit has received little scientific attention. This study sheds new light on the deposit by characterising it and providing insights into carbon sequestration and carbon-hydrogen interactions in the continental crust. This study infers that the Amitsoq graphite deposit formed between 1793-1762 Ma, shortly after the emplacement of the Julianehåb batholith. The erosion of the batholith generated the sediments that subsequently transformed the pelite, which hosts the ore (Garde et al., 2002). A strong biogenic production and conservation, which characterised the Paleoproterozoic (Parnell et al., 2021), provided the carbonaceous material that was then transformed into graphite through high-temperature, low-pressure metamorphism. The exact process by which the graphite was formed is still unknown, but this study proposes plausible mechanisms through which a fluid produced by the metamorphism of a pelite could precipitate high amounts of graphite, with ratios of up to 1 mol of graphite every 10 mol of fluid in the case of an almost complete dehydration (95%) of a fluid with carbon activity of 1 and log fO_2 of -21.45.

The petrographic observations led to the identification of the main mineral phases and textures, highlighting the abundance of alteration in most of the analysed lithologies. The granitoid bodies are mostly granodiorites with varying content of amphiboles or biotite. Despite having different ages, they show similar characteristics, suggesting a possible relationship between the Ilua plutonic suite granites, emplaced from 1755-1723 Ma, and the older Julianehåb batholith (1850-1750 Ma; Chadwick & Garde, 1996). The ore exhibits a tightly folded structure similar to those described for the D_1-D_2 metamorphic event that characterised the Ketilidian orogeny. It is a heterogeneous graphitic-sulphidic quartzo-

feldspathic schist, composed of graphite, pyrrhotite, quartz, and variable amounts of biotite and feldspars, with biotite and graphite defining the foliation. The host rock displays different compositions but can be regarded as a pelitic gneiss, and some samples from the host, not necessarily the ones closest to the ore, show the presence of graphite flakes.

Electron microprobe analysis allowed to assess the composition of minerals, identifying trace minerals such as uraninite and monazite, and providing data for thermometry calculations that, in the case of garnet-biotite thermometer (Ferry & Spear, 1978; Ganguly et al., 1996) yielded ∼500 °C as equilibrium temperature.

$\delta^{13}C$ analysis yielded very narrow results, between -32‰ and - 33‰, this allowed to infer that the carbon present in the Amitsoq graphite deposit most probably originated from biological processes or transformation of biogenic material.

Raman spectroscopy analysis led to two remarkable results, the first is the thermometric estimation of peak metamorphic temperature of graphite in the host rock, which was estimated at 575 °C using thermometer from Beyssac et al. (2002) the second is the presence of hydrogen in fluid inclusions in the ore.

This case study shows that graphite precipitation is a natural and effective way with which CO_2 may be stored in crustal rocks over geologically significant time scales, therefore reducing the content of greenhouse gases in the atmosphere, and possibly providing a baseline for carbon storage techniques. Despite the effectiveness of this process, though, it is important to note that the interaction of graphite and hydrogen leads to the generation of methane (Vitale Brovarone et al., 2017; Pena-Alvarez et al., 2021).

This may pose a problem since methane is a more effective greenhouse gas than carbon dioxide (Howart, 2014), possibly making the hypothesis of applying this process for carbon storage less appealing.

Although this study provides significant advances in the knowledge of the deposit, there is still more to be better understood, both in terms of how the deposit exactly formed and whether the late-stage processes that likely formed the observed hydrogen were effective enough to produce significant amounts of hydrogen. Future work will assess the exact age of graphite mineralisation through Re-Os dating. Moreover, the samples from the ore all come from the same region of the ore body, a wider distribution of sample could lead to identification of differences within the ore body that may help in the identification of the deposition process. A fair number of samples from the hostrock was analysed and what is treated as a single rock unit, in reality displays significant differences. This is because, as it is possible to see in Figure 8, the geographical distribution is wide, and the influence of nearby pluton emplacement may have altered the original mineralogy of samples, affecting the observations. Therefore, a new sampling campaign could provide new insights on the history of the hostrock. Other than this, more thermometric analysis could further confirm the few calculations made in this thesis.

8. References

Ahluwalia, R. K., & Peng, J. K. (2009). Automotive hydrogen storage system using cryo-adsorption on activated carbon. International Journal of Hydrogen Energy, 34(13), 5476-5487.

Allaart, J. H. (1975). Geologiske kort over Grønland, 1: 500 000, sheet 1, Sydgrønland. Grønlands Geologiske Undersøgelse, Copenhagen.

Anthony, J. W., Bideaux, R. A., Bladh, K. W., & Nichols, M. C. (1990). Handbook of mineralogy: volume I. elements, sulfides, sulfosalts. Mineralogical Society of America. Chantilly, Virginia.

Balat M. (2008) Potential importance of hydrogen as a future solution to environmental and transportation problems. Int J Hydrogen Energy; 33:4013–29.

Ball, S. H. (1923). The mineral resources of Greenland.

Bau, M. (1991). Rare-earth element mobility during hydrothermal and metamorphic fluid-rock interaction and the significance of the oxidation state of europium. Chemical Geology, 93(3-4), 219-230.

Bau, M., & Moller, P. (1991). REE systematics as source of information on minerogenesis. In 25 years, Society for Geology applied to Mineral Deposits, anniversary meeting (pp. 17-20).

Bebout, G. E., Cooper, D. C., Bradley, A. D., & Sadofsky, S. J. (1999). Nitrogen-isotope record of fluid-rock interactions in the Skiddaw Aureole and granite, English Lake District. American Mineralogist, 84(10), 1495-1505.

Bell, R. M., Kolb, J., Waight, T. E., Bagas, L., & Thomsen, T. B. (2017). A Palaeoproterozoic multi-stage hydrothermal alteration system at Nalunaq gold deposit, South Greenland. Mineralium Deposita, 52, 383-404.

Bell, R. M., Kolb, J., & Waight, T. E. (2018). Assessment of lithological, geochemical and structural controls on gold distribution in the Nalunaq gold deposit, South Greenland using three-dimensional implicit modelling. Geological Society, London, Special Publications, 453(1), 385-405.

Bergfeld D., Nabelek P. I. and Labotka T. C. (1996) Carbon isotope exchange during polymetamorphism in the Panamint Mountains, California. J. Metam. Geol. 14, 199–212.

Berrangé, J. P. (1970). The geology of two small layered hornblende peridotite (picrite) plutons in South Greenland. CA Reitzel.

Berthelsen, A., & Henriksen, N. (1975). Geological map of Greenland 1: 100 000 Ivigtut 61 V. 1 Syd [South]: The orogenic and cratogenic geology of a precambrian shield area. Meddelelser om Groenland (Denmark). v. 186 (1).

Berthelsen, A., & Noe-Nygaard, A. (1965). The Precambrian of Greenland. The Precambrian, 2, 113-262.

Berner, R. A. (1970). Sedimentary pyrite formation. American journal of science, 268(1), 1-23.

Beyssac, O., Goffé, B., Chopin, C., & Rouzaud, J. N. (2002). Raman spectra of carbonaceous material in metasediments: a new geothermometer. Journal of metamorphic Geology, 20(9), 859-871.

Blumenberg, M., Thiel, V., Riegel, W., Kah, L. C., & Reitner, J. (2012). Biomarkers of black shales formed by microbial mats, Late Mesoproterozoic (1.1 Ga) Taoudeni Basin, Mauritania. Precambrian Research, 196, 113-127.

Blundy, J. D., & Holland, T. J. (1990). Calcic amphibole equilibria and a new amphibole-plagioclase geothermometer. Contributions to mineralogy and petrology, 104(2), 208-224.

Boesen, C., & Postma, D. (1988). Pyrite formation in anoxic environments of the Baltic. American Journal of Science, 288(6), 575-603.

Bondam, J. (1992). Graphite occurrences in Greenland: a review. Grønlands Geologiske Undersøgelse.

Bondesen, E. (1970). The stratigraphy and deformation of the Precambrian rocks of the Grænseland area, South-West Greenland.

Bondesen, E., & Henriksen, N. (1965). On some pre-Cambrian metadolerites from the central Ivigtut region SW Greenland. Bulletin Grønlands Geologiske Undersøgelse, 52, 1-42.

Brown, P. E., Dempster, T. J., Harrison, T. N., & Hutton, D. H. W. (1992). The rapakivi granites of S Greenland—crustal melting in response to extensional tectonics and magmatic underplating. Earth and Environmental Science Transactions of the Royal Society of Edinburgh, 83(1-2), 173-178.

Brown, P. E., Fallick, A. E., Becker, S. M., Dempster, T. J., & Hutton, D. H. W. (1999). The Rapakivi granites of South Greenland—stable isotope characteristics of their black and white facies and the nature of their protolith. Lithos, 46(3), 485-504.

Chadwick, B., Dawes, P. R., Escher, J. C., Friend, C. R. L., Hall, R. P., Kalsbeek, F., ... & Vasudev, V. N. (1989). The Proterozoic mobile belt in the Ammassalik region, South-East Greenland (Ammassalik mobile belt): an introduction and re-appraisal. Rapport Grønlands geologiske Undersøgelse, 146, 5-12.

Chadwick, B., & Garde, A. A. (1996). Palaeoproterozoic oblique plate convergence in South Greenland: a reappraisal of the Ketilidian Orogen. Geological Society, London, Special Publications, 112(1), 179-196.

Chadwick, B., Garde, A. A., Grocott, J., McCaffrey, K. J., & Hamilton, M. A. (2000). Ketilidian structure and the rapakivi suite between Lindenow Fjord and Kap Farvel, South-east Greenland. Geology of Greenland Survey Bulletin, 186, 50-59.

Chadwick, B., Garde, A. A., Grocott, J., Swager, C., Wardle, R. J., & Hall, J. (1997). Batholith–forearc structure in the Palaeoproterozoic Ketilidian orogen, South-East Greenland. In Lithoprobe Eastern Canadian Shield Onshore–Offshore Transect (ECSOOT): report of 1997 transect meeting. Compiled by RJ Wardle and J. Hall. Lithoprobe Report (No. 61, pp. 27-35).

Crawford, M. L., & Hollister, L. S. (1986). Metamorphic fluids: the evidence from fluid inclusions. In Fluid—Rock Interactions during Metamorphism (pp. 1-35). New York, NY: Springer New York.

Condie, K. C., Des Marais, D. J., & Abbott, D. (2001). Precambrian superplumes and supercontinents: a record in black shales, carbon isotopes, and paleoclimates?. Precambrian Research, 106(3-4), 239-260.

Connolly, J. A. D. (1995). Phase diagram methods for graphitic rocks and application to the system C− O− H− FeO− TiO2− SiO2. Contributions to Mineralogy and Petrology, 119(1), 94-116.

Condie, K. C. (2014). Growth of continental crust: a balance between preservation and recycling. Mineralogical Magazine, 78(3), 623-637.

Connolly, J. A. D., & Cesare, B. (1993). C-O-H-S fluid composition and oxygen fugacity in graphitic metapelites. Journal of metamorphic geology, 11(3), 379-388.

Deines, P., Harris, J. W., Robinson, D. N., Gurney, J. J., & Shee, S. R. (1991). Carbon and oxygen isotope variations in diamond and graphite eclogites from Orapa, Botswana, and the nitrogen content of their diamonds. Geochimica et Cosmochimica Acta, 55(2), 515-524.

Dempster, T. J., Harrison, T. N., Brown, P. E., & Hutton, D. H. (1991). Low-pressure granulites from the Ketilidian Mobile Belt of southern Greenland. Journal of Petrology, 32(5), 979-1004.

Drobner, E., Huber, H., Wächtershäuser, G., Rose, D., & Stetter, K. O. (1990). Pyrite formation linked with hydrogen evolution under anaerobic conditions. Nature, 346(6286), 742-744.

Duke, E. F., Galbreath, K. C., & Trusty, K. J. (1990). Fluid inclusion and carbon isotope studies of quartz-graphite veins, Black Hills, South Dakota, and Ruby Range, Montana. Geochimica et Cosmochimica Acta, 54(3), 683-698.

Dunn, S. (2002). Hydrogen futures: toward a sustainable energy system. International journal of hydrogen energy, 27(3), 235-264.

Elderfield, H., Upstill-Goddard, R., & Sholkovitz, E. R. (1990). The rare earth elements in rivers, estuaries, and coastal seas and their significance to the composition of ocean waters. Geochimica et Cosmochimica Acta, 54(4), 971-991.

Escher, A. (1966). The Deformation and Granitisation of Ketilidian Rocks in the Nanortalik Area, S. Greenland: Thèse Présentée À la Faculté Des Sciences de L'Université de Lausanne Pour Obtenir Le Grade de Docteur Ès Sciences (Doctoral dissertation, Bianco Luno).

European Commission, (2020) Critical Raw Materials Resilience: Charting a Path towards greater Security and Sustainability

Ferry, J. T., & Spear, F. S. (1978). Experimental calibration of the partitioning of Fe and Mg between biotite and garnet. Contributions to mineralogy and petrology, 66(2), 113-117.

Frezzotti, M. L., Tecce, F., & Casagli, A. (2012). Raman spectroscopy for fluid inclusion analysis. Journal of Geochemical Exploration, 112, 1-20.

Frost, B. R. (1979). Mineral equilibria involving mixed-volatiles in a COH fluid phase; the stabilities of graphite and siderite. American Journal of Science, 279(9), 1033-1059.

Ganguly, J. (1979). Garnet and clinopyroxene solid solutions, and geothermometry based on Fe-Mg distribution coefficient. Geochimica et Cosmochimica Acta, 43(7), 1021-1029.

Ganguly, J., Cheng, W., & Tirone, M. (1996). Thermodynamics of aluminosilicate garnet solid solution: new experimental data, an optimized model, and thermometric applications. Contributions to Mineralogy and Petrology, 126, 137-151.

Garde, A. A., Chadwick, B., Grocott, J., & Swager, C. (1997). Metasedimentary rocks, intrusions and deformation history in the south-east part of the c. 1800 Ma Ketilidian orogen, South Greenland: Project SUPRASYD 1996. Geology of Greenland Survey Bulletin, 176, 60-65.

Garde, A. A., Chadwick, B., Grocott, J., & Swager, C. P. (1998). GEUS Lindenow Fjord 60 Ø. 1 NORD. Geological Survey of Denmark and Greenland.

Garde, A. A., Chadwick, B., Grocott, J., Hamilton, M. A., McCaffrey, K. J., & Swager, C. P. (2002). Mid-crustal partitioning and attachment during oblique convergence in an arc system, Palaeoproterozoic Ketilidian orogen, southern Greenland. Journal of the Geological Society, 159(3), 247-261.

Garde, A. A., Hamilton, M. A., Chadwick, B., Grocott, J., & McCaffrey, K. J. W. (2002). The Ketilidian orogen of South Greenland: geochronology, tectonics, magmatism, and fore-arc accretion during Palaeoproterozoic oblique convergence. Canadian Journal of Earth Sciences, 39(5), 765-793.

Garside, M., (2023) https://www.statista.com/statistics/1005851/global-graphite-production/ retrieved 20/02/2023.

Goodenough, K. M., Krabbendam, M., Shaw, R. A., & Crowley, Q. G. (2013). Making and breaking Columbia (Nuna): formation of a critical metal province? A North Atlantic view.

Grocott, J., Garde, A. A., Chadwick, B., Cruden, A. R., & Swager, C. (1999). Emplacement of rapakivi granite and syenite by floor depression and roof uplift in the Palaeoproterozoic Ketilidian orogen, South Greenland. Journal of the Geological Society, 156(1), 15-24.

Guidotti, C. V., Teichmann, F., & Henry, D. J. (1991). Chlorite-bearing polymetamorphic metapelites in the Rangeley area, Maine: Evidence for equilibrium assemblages. American Mineralogist, 76(5-6), 867-869.

Gumsley, A. P., Chamberlain, K. R., Bleeker, W., Söderlund, U., De Kock, M. O., Larsson, E. R., & Bekker, A. (2017). Timing and tempo of the Great Oxidation Event. Proceedings of the National Academy of Sciences, 114(8), 1811-1816.

Hall, A. J. (1986). Pyrite-pyrrhotine redox reactions in nature. Mineralogical Magazine, 50(356), 223-229.

Hamilton, M. A., Garde, A. A., Chadwick, B., Swager, C., Wardle, J. R., & Hall, J. (1996). Observations on Palaeoproterozoic fore-arc sedimentation and deformation: preliminary U-Pb results from the Ketilidian orogen, South Greenland. In Lithoprobe Eastern Canadian Shield Onshore–Offshore Transect (ESCOOT), Report of 1996 Transect meeting. University of British Columbia, Lithoprobe Report (Vol. 57, pp. 112-122).

Henry, D. J., & Guidotti, C. V. (2002). Titanium in biotite from metapelitic rocks: Temperature effects, crystal-chemical controls, and petrologic applications. American Mineralogist, 87(4), 375-382.

Harry, W. T., & Soen, O. I. (1964). The pre-cambrian basement of Alángorssuaq, South Greenland and its copper mineralization at Josvaminen: Grønlands geologiske undersøgelse. Reitzel.

Henriksen, N. (1969). Chemical relations between metabasaltic lavas and metadolerites in the Ivigtut area, South-West Greenland. Fr. Bagges Kgl. Hofbogtrykkeri.

Higgins, A. K., (1970). The stratigraphy and structure of the Ketilidian rocks of Midternæs, South-West Greenland. Grønlands Geologiske Undersøgelse, 87.

Higgins, A. K., Dawes, P. R., & Kalsbeek, F. (1970). The Plutonic History of the Tassiussaq Area, South Greenland: With Special Reference to a High-grade Gneiss Complex (Vol. 189, No. 1). CA Reitzel.

Hirsch, D. (2023) https://serc.carleton.edu/research_education/equilibria/reactioncurves.html#nettransfer retrieved 01/07/2023

Ho, E. S., Meyers, P. A., & Mauk, J. L. (1990). Organic geochemical study of mineralization in the Keweenawan Nonesuch Formation at White Pine, Michigan. Organic Geochemistry, 16(1-3), 229-234.

Holland, T., & Blundy, J. (1994). Non-ideal interactions in calcic amphiboles and their bearing on amphibole-plagioclase thermometry. Contributions to mineralogy and petrology, 116, 433-447.

Howarth, R. W. (2014). A bridge to nowhere: methane emissions and the greenhouse gas footprint of natural gas. *Energy Science & Engineering*, *2*(2), 47-60.

Huff, T. A., & Nabelek, P. I. (2007). Production of carbonic fluids during metamorphism of graphitic pelites in a collisional orogen—an assessment from fluid inclusions. Geochimica et Cosmochimica Acta, 71(20), 4997-5015.

Hurai, V., Simon, K., & Bezák, V. (1997). Contrasting chemistry and H, O, C isotope composition of greenschist-facies, Hercynian and Alpine metamorphic fluids (Western Carpathians). Chemical geology, 136(3-4), 281-293.

Hutton, D. H. (1988). Granite emplacement mechanisms and tectonic controls: inferences from deformation studies. Earth and Environmental Science Transactions of the Royal Society of Edinburgh, 79(2-3), 245-255.

Ivy J. (2004) Summary of electrolytic hydrogen production: milestone completion report, NREL/MP-560-36734. National Renewable Energy Laboratory, USA, Tech. Rep. NREL/MP-560-36734.

Javoy, M., Pineau, F., & Delorme, H. (1986). Carbon and nitrogen isotopes in the mantle. Chemical geology, 57(1-2), 41-62.

Johnston, D. T., Farquhar, J., Summons, R. E., Shen, Y., Kaufman, A. J., Masterson, A. L., & Canfield, D. E. (2008). Sulfur isotope biogeochemistry of the Proterozoic McArthur Basin. Geochimica et Cosmochimica Acta, 72(17), 4278-4290.

Jørgensen, B. B. (1989). Sulfate reduction in marine sediments from the Baltic Sea-North Sea transition. Ophelia, 31(1), 1-15.

Jørgensen, C., & Ropenus, S. (2008). Production price of hydrogen from grid connected electrolysis in a power market with high wind penetration. International journal of hydrogen energy, 33(20), 5335-5344.

Kalsbeek, F., & Taylor, P. N. (1985). Isotopic and chemical variation in granites across a Proterozoic continental margin—the Ketilidian mobile belt of South Greenland. Earth and Planetary Science Letters, 73(1), 65-80.

Kaltoft, K., Schlatter, D. M., & Kludt, L. (2000). Geology and genesis of Nalunaq Palaeoproterozoic shear zone-hosted gold deposit, South Greenland. Applied Earth Science, 109(1), 23-33.

Kita, I., Matsuo, S., & Wakita, H. (1982). H2 generation by reaction between H2O and crushed rock: an experimental study on H2 degassing from the active fault zone. Journal of Geophysical Research: Solid Earth, 87(B13), 10789-10795.

Kolb, J., Keiding, J. K., Steenfelt, A., Secher, K., Keulen, N., Rosa, D., & Stensgaard, B. M. (2016). Metallogeny of Greenland. Ore Geology Reviews, 78, 493-555.

Lin, L. H., Hall, J., Lippmann-Pipke, J., Ward, J. A., Sherwood Lollar, B., DeFlaun, M., ... & Onstott, T. C. (2005a). Radiolytic H2 in continental crust: nuclear power for deep subsurface microbial communities. Geochemistry, Geophysics, Geosystems, 6(7).

Lin, L. H., Slater, G. F., Lollar, B. S., Lacrampe-Couloume, G., & Onstott, T. C. (2005b). The yield and isotopic composition of radiolytic H2, a potential energy source for the deep subsurface biosphere. Geochimica et Cosmochimica Acta, 69(4), 893-903.

Luque, F. J., Ortega, L., Barrenechea, J. F., Millward, D., Beyssac, O., & Huizenga, J. M. (2009). Deposition of highly crystalline graphite from moderate-temperature fluids. Geology, 37(3), 275-278.

Luque, F. J., Crespo-Feo, E., Barrenechea, J. F., & Ortega, L. (2012). Carbon isotopes of graphite: Implications on fluid history. Geoscience Frontiers, 3(2), 197-207.

McDowall W, Eames M. (2006). Forecasts, scenarios, visions, backcasts and roadmaps to the hydrogen economy: a review of the hydrogen futures literature. Energy Policy; 34:1236–50.

Martin, A. P., Prave, A. R., Condon, D. J., Lepland, A., Fallick, A. E., Romashkin, A. E., ... & Rychanchik, D. V. (2015). Multiple Palaeoproterozoic carbon burial episodes and excursions. Earth and Planetary Science Letters, 424, 226-236.

Mazloomi, K., & Gomes, C. (2012). Hydrogen as an energy carrier: Prospects and challenges. Renewable and Sustainable Energy Reviews, 16(5), 3024-3033.

Melezhik, V. A., Fallick, A. E., Martin, A. P., Condon, D. J., Kump, L. R., Brasier, A. T., & Salminen, P. E. (2013). 7.3 the Palaeoproterozoic perturbation of the global carbon cycle: the Lomagundi-Jatuli isotopic event. Reading the Archive of Earth's Oxygenation: Volume 3: Global Events and the Fennoscandian Arctic Russia-Drilling Early Earth Project, 1111-1150.

Melezhik, V. A., Huhma, H., Condon, D. J., Fallick, A. E., & Whitehouse, M. J. (2007). Temporal constraints on the Paleoproterozoic Lomagundi-Jatuli carbon isotopic event. Geology, 35(7), 655-658.

Momirlan, M., & Veziroglu, T. N. (2005). The properties of hydrogen as fuel tomorrow in sustainable energy system for a cleaner planet. International journal of hydrogen energy, 30(7), 795-802.

Muhammed, N. S., Haq, B., Al Shehri, D., Al-Ahmed, A., Rahman, M. M., & Zaman, E. (2022). A review on underground hydrogen storage: Insight into geological sites, influencing factors and future outlook. *Energy Reports*, *8*, 461-499.

Mullis, J. (1987). Fluid inclusion studies during very low-grade metamorphism. Low temperature metamorphism, 162-199.

Nakamura, N. (1974). Determination of REE, Ba, Fe, Mg, Na and K in carbonaceous and ordinary chondrites. Geochimica et cosmochimica acta, 38(5), 757-775.

Nielsen, H. (1979). Sulfur isotopes. In Lectures in isotope geology (pp. 283-312). Springer Berlin Heidelberg.

Olsen, S. N., & Ferry, J. M. (1995). A comparative fluid inclusion study of the Waterville and Sangerville (Vassalboro) Formations, south-central Maine. Contributions to Mineralogy and Petrology, 118, 396-413.

Gregorio Padro CE, Lau F (2002). Advances in hydrogen energy. New York: Kluwer Academic Publishers.

Jasinski, S. M. (2012). Mineral commodity summaries. US Geological Survey (ed), 118-119.

Ohmoto, H., & Kerrick, D. M. (1977). Devolatilization equilibria in graphitic systems. American Journal of Science, 277(8), 1013-1044.

Parfrey, L. W., Lahr, D. J., Knoll, A. H., & Katz, L. A. (2011). Estimating the timing of early eukaryotic diversification with multigene molecular clocks. Proceedings of the National Academy of Sciences, 108(33), 13624-13629.

Park, R. G. (1994). Early Proterozoic tectonic overview of the northern British Isles and neighbouring terrains in Laurentia and Baltica. Precambrian Research, 68(1-2), 65-79.

Parnell, J., Brolly, C., & Boyce, A. J. (2021). Graphite from Palaeoproterozoic enhanced carbon burial, and its metallogenic legacy. Geological Magazine, 158(9), 1711-1718.

Persoz, F. (1969). Evolution plutonique et structurale de la presqu'ile d'Akuliaruseq. Groenland meridional: Grönland, Bd, 175.

Paterson, S. R., Vernon, R. H., & Tobisch, O. T. (1989). A review of criteria for the identification of magmatic and tectonic foliations in granitoids. Journal of structural geology, 11(3), 349-363.

Petersen, J. S., Kaltoft, K., & Schlatter, D. (1997). The Nanortalik gold district in South Greenland. Mineral deposits: research and exploration. Where do they meet, 285-288.

Patino Douce, A. E., Johnston, A. D., & Rice, J. M. (1993). Octahedral excess mixing properties in biotite: a working model with applications to geobarometry and geothermometry. American Mineralogist, 78(1-2), 113-131.

Peña-Alvarez, M., Brovarone, A. V., Donnelly, M. E., Wang, M., Dalladay-Simpson, P., Howie, R., & Gregoryanz, E. (2021). In-situ abiogenic methane synthesis from diamond and graphite under geologically relevant conditions. *Nature Communications*, *12*(1), 6387.

Powell, R., & Holland, T. J. B. (2008). On thermobarometry. Journal of Metamorphic Geology, 26(2), 155-179.

Rumble III, D., Duke, E. F., & Hoering, T. L. (1986). Hydrothermal graphite in New Hampshire: evidence of carbon mobility during regional metamorphism. Geology, 14(6), 452-455.

Rumble III, D., & Hoering, T. C. (1986). Carbon isotope geochemistry of graphite vein deposits from New Hampshire, USA. Geochimica et Cosmochimica Acta, 50(6), 1239-1247.

Sadofsky, S. J., & Bebout, G. E. (2000). Ammonium partitioning and nitrogen-isotope fractionation among coexisting micas during high-temperature fluid-rock interactions: Examples from the New England Appalachians. Geochimica et Cosmochimica Acta, 64(16), 2835-2849.

Schidlowski, M. (1988). A 3,800-million-year isotopic record of life from carbon in sedimentary rocks. Nature, 333(6171), 313-318.

Schidlowski, M. (2001). Carbon isotopes as biogeochemical recorders of life over 3.8 Ga of Earth history: evolution of a concept. Precambrian Research, 106(1-2), 117-134.

Schlapbach, L., & Borgschulte, A. (2008). Hydrogen as a Future Energy Carrier. Wiley-VCH.

Schlesinger WH (1997) Biogeochemistry. An analysis of global change, 2nd edn. Academic, San Diego

Schoots K, Ferioli F, Kramer GJ, van der Zwaan BCC (2008). Learning curves for hydrogen production technology: an assessment of observed cost reductions. Int J Hydrogen Energy.

Schønwandt, H.K., (1971). Mineralised ultramafic rocks in South Greenland. Rapp. Grønl. Geol. Unders. 35, 30–31.

Schulte, M., Blake, D., Hoehler, T., & McCollom, T. (2006). Serpentinization and its implications for life on the early Earth and Mars. Astrobiology, 6(2), 364-376.

Schwab, V., Spangenberg, J. E., & Grimalt, J. O. (2005). Chemical and carbon isotopic evolution of hydrocarbons during prograde metamorphism from 100 C to 550 C: Case study in the Liassic black shale formation of Central Swiss Alps. Geochimica et Cosmochimica Acta, 69(7), 1825-1840.

Seal RR, Alpers CN, Rye RO (2000) Stable isotope systematics of sulfate minerals. Rev Mineral Geochem 40:541–602

Secher, K., & Stendal, H. (2010). Greenland'snickelresourcepotential. Geology and Ore, 17, 1-12.

Seewald, J. S. (2001). Aqueous geochemistry of low molecular weight hydrocarbons at elevated temperatures and pressures: constraints from mineral buffered laboratory experiments. Geochimica et Cosmochimica Acta, 65(10), 1641-1664.

Sherwood Lollar, B., Voglesonger, K., Lin, L. H., Lacrampe-Couloume, G., Telling, J., Abrajano, T. A., ... & Pratt, L. M. (2007). Hydrogeologic controls on episodic H2 release from Precambrian fractured rocks—energy for deep subsurface life on Earth and Mars. Astrobiology, 7(6), 971-986.

Sherwood Lollar, B., Onstott, T. C., Lacrampe-Couloume, G., & Ballentine, C. J. (2014). The contribution of the Precambrian continental lithosphere to global H2 production. Nature, 516(7531), 379-382.

Sleep, N. H., Meibom, A., Fridriksson, T., Coleman, R. G., & Bird, D. K. (2004). H2-rich fluids from serpentinization: geochemical and biotic implications. Proceedings of the National Academy of Sciences, 101(35), 12818-12823.

Spinks, J. W., & Woods, R. J. (1990). An introduction to radiation chemistry.

Steenfelt, A., Kolb, J., & Thrane, K. (2016). Metallogeny of South Greenland: a review of geological evolution, mineral occurrences and geochemical exploration data. Ore Geology Reviews, 77, 194-245.

Steenfelt, A., & Schjøth, F. (2005). Use of stream sediment and lithological data to estimate the chemical compositions of three land areas in South Greenland. GEUS, Geological Survey of Denmark and Greenland.

Stevens, T. O., & McKinley, J. P. (1995). Lithoautotrophic microbial ecosystems in deep basalt aquifers. Science, 270(5235), 450-455.

Strauss, H., Melezhik, V. A., Lepland, A., Fallick, A. E., Hanski, E. J., Filippov, M. M., ... & Brasier, A. T. (2013). 7.6 Enhanced accumulation of organic matter: the shunga event. Reading the Archive of Earth's Oxygenation: Volume 3: Global Events and the Fennoscandian Arctic Russia-Drilling Early Earth Project, 1195-1273.

St-Onge, M. R., Van Gool, J. A., Garde, A. A., & Scott, D. J. (2009). Correlation of Archaean and Palaeoproterozoic units between northeastern Canada and western Greenland: constraining the pre-collisional upper plate accretionary history of the Trans-Hudson orogen. Geological Society, London, Special Publications, 318(1), 193-235.

Sverjensky, D. A. (1984). Europium redox equilibria in aqueous solution. Earth and Planetary Science Letters, 67(1), 70-78.

Taylor, H.A., Jr., (2006). Graphite. Industrial Minerals and Rocks. Society for Mining, Metallurgy, and Exploration, Inc., Littleton, Colorado, pp. 507-518

Touret, J. L. R. (2001). Fluids in metamorphic rocks. Lithos, 55(1-4), 1-25.

Van Breemen, O., Aftalion, M., & Allaart, J. H. (1974). Isotopic and geochronologic studies on granites from the Ketilidian mobile belt of South Greenland. Geological Society of America Bulletin, 85(3), 403-412.

Van Kranendonk, M. J., St-Onge, M. R., & Henderson, J. R. (1993). Paleoproterozoic tectonic assembly of Northeast Laurentia through multiple indentations. Precambrian Research, 63(3-4), 325-347.

Verhelst, S., & Wallner, T. (2009). Hydrogen-fueled internal combustion engines. Progress in energy and combustion science, 35(6), 490-527.

Viljoen, K. S. (1995). Graphite-and diamond-bearing eclogite xenoliths from the Bellsbank kimberlites, Northern Cape, South Africa. Contributions to Mineralogy and Petrology, 121, 414-423.

Vitale Brovarone, A., Martinez, I., Elmaleh, A., Compagnoni, R., Chaduteau, C., Ferraris, C., & Esteve, I. (2017). Massive production of abiotic methane during subduction evidenced in metamorphosed ophicarbonates from the Italian Alps. *Nature Communications, 8*(1), 14134.

Wallis, R. H. (1966). The Geology of North-east Tasermiut Fjord South Greenland (Doctoral dissertation, University of Birmingham).

Walther, J. V., & Orville, P. M. (1982). Volatile production and transport in regional metamorphism. Contributions to Mineralogy and Petrology, 79, 252-257.

Watterson, J. (1968). Plutonic Development of the Ilordleq Area, South Greenland: Part 2: Late-kinematic Basic Dykes. CA Reitzel.

Wegmann, E. (1938). Geological Investigations in Southern Greenland: Geologiske Undersøgelser Y Sydgrønland. On the Structural Divisions of Southern Grönland. Reitzel.

White, W. M. (2005). Geochemistry. An on-line textbook. Cornell University, 701.

Whitney, D., (2023) https://serc.carleton.edu/research_education/equilibria/classicalthermobarometry.html retrieved 30/06/2023

Wissler, M. (2006). Graphite and carbon powders for electrochemical applications. Journal of power sources, 156(2), 142-150.

Wolfe, J. M., & Fournier, G. P. (2018). Horizontal gene transfer constrains the timing of methanogen evolution. Nature ecology & evolution, 2(5), 897-903.

Wopenka, B., & Pasteris, J. D. (1993). Structural characterization of kerogens to granulite-facies graphite: applicability of Raman microprobe spectroscopy. American mineralogist, 78(5-6), 533-557.

Zhao, G., Sun, M., Wilde, S. A., & Li, S. (2004). A Paleo-Mesoproterozoic supercontinent: assembly, growth and breakup. Earth-Science Reviews, 67(1-2), 91-123.

9. Acknowledgements

This study largely benefitted from sampling campaigns performed in in the studied area by GreenRoc Mining Plc, by Tod Waight and Rikke Vestergaard and by Tod Waight and Katrine Baden.

I would like to express my gratitude to all the people who contributed to this work and supported me throughout my thesis and the entire duration of this master's program. First, I would like to thank my supervisor, Professor Alberto Vitale Brovarone, for his constant support, patience, and genuine interest in the project.

I am grateful to Stefan Bernstein and GreenRoc Mining Plc for providing me with the opportunity to study and gain experience on such an interesting and complex project.

I would also like to extend my thanks to Kristoffer Szilas, Sampriti Basak, Maja Bar Rasmussen, and the Early Earth Research Group for hosting me at the University of Copenhagen and for teaching me a lot and for providing assistance during my internship.

I am grateful to EIT Raw Materials for providing many growth opportunities throughout these two years of my master's program.

Lastly, I would like to thank all my friends and family for their unwavering support.